Doppler Shifts in the KATRIN Experiment

by

Matthew K. Heine

Submitted to the Department of Physics
in partial fulfillment of the requirements for the degree of

Bachelor of Science in Physics

at the

MASSACHUSETTS INSTITUTE OF TECHNOLOGY

June 2008

©Matthew K. Heine All Rights Reserved

Author ....
Department of Physics
May 9, 2008

Certified by ....
Joseph Formaggio
Assistant Professor
Thesis Supervisor

Accepted by ....
David Pritchard
Chairman, Department Thesis Committee

MASSACHUSETTS INSTITUTE
OF TECHNOLOGY
JUN 1 3 2008
LIBRARIES
ARCHIVES

Doppler Shifts in the KATRIN Experiment

by

Matthew K. Heine

Submitted to the Department of Physics
on May 9, 2008, in partial fulfillment of the
requirements for the degree of
Bachelor of Science in Physics

Abstract

In the past few decades, neutrinos, which are predicted to be massless particles by the Standard Model of Particle Physics, have been shown to have non-zero mass. The absolute scale of this neutrino mass has significant implications in particle physics, astrophysics, and cosmology. The KATRIN experiment is designed to measure this absolute scale by examining the beta decay spectrum of molecular, gaseous tritium source. In this thesis, the beta decay of this molecular tritium is simulated to study the effects of "Doppler shifts" in the energy of the emitted electrons due to the random thermal motion and fluid flow velocity of the differentially pumped tritium gas. Simulated spectra are presented for three different neutrino masses and the relative effects of the thermal and flow velocities are discussed.

Thesis Supervisor: Joseph Formaggio
Title: Assistant Professor

Acknowledgments

I would like to thank Asher Kaboth for allowing me to use his fitter, and for all the time and effort he invested into adapting his fitter for my purposes and getting it running. I would also like to thank him for his generous help throughout the project. I would like to thank Sarah Trowbridge for her efforts and assistance during this project. Furthermore, I would like to thank Professor Felix Sharipov for his very helpful and timely correspondences and for sending me data. And last, but not least, I would like to thank Professor Joseph Formaggio for giving me the opportunity to work on this project and to see the experiment in person.

Contents

1 Massive Neutrinos **13**

1.1 The Discovery of the Neutrino 13

1.2 Motivation for a Non-Zero Neutrino Mass: Neutrino Oscillations . . . 15

1.3 The Impact of the Neutrino Mass Scale 18

2 The KATRIN Experiment **21**

2.1 The Theory 21

2.2 The Status of Neutrino Mass Determination 23

2.3 Advantages of KATRIN 24

2.4 The KATRIN Setup 25

2.4.1 Experimental Overview 26

2.4.2 The WGTS in Detail 29

3 Beta Decay **31**

3.1 Fermi's Golden Rule 31

3.2 Tritium Beta Decay 32

3.3 The Fermi Function 33

3.4 The Kurie Plot 35

3.5 Molecular Decay and Final State Distribution 37

4 Thermal Motion and Doppler Shifts **41**

5 Velocity Profile Due to Pumping **45**

5.1 The Density/Pressure Profile 45

5.2 The Viscosity of Tritium 49
5.3 The Velocity Profile 51
    5.3.1 The Navier-Stokes Equation 51
    5.3.2 The Boltzmann Transport Equation 52
    5.3.3 Boundary Conditions 53

6 Results & Analysis **57**
6.1 The Density and Velocity Profiles 57
6.2 The Beta Spectra 57
    6.2.1 Inclusion of the Final State Distribution 59
    6.2.2 Interpretation of These Results 66
6.3 The Integrated Spectra and Fit Results 68

7 Conclusions **73**

A Simulation Code **75**

List of Figures

1-1 The Beta Decay Spectrum of molecular tritium, T_2. Note that this coninuous energy spectrum is inconsistent with momentum/energy conservation in a 2-body decay. This histogram was constructed from the stationary decay data in Fig. 6.2.1 and so, corresponds to a electron antineutrino mass of 1eV/c^2. 14

1-2 The impact of the neutrino mass scale on the question of hierarchical or degenerate neutrino masses. Plotted are the neutrino mass eigenvalues (m1<m2<m3) as a function of the value of the lightest eigenvalue, m1. One can see that a positive identification of a neutrino mass *above* $\sim$ 0.1eV would clearly indicate a quasi-degenerate mass scheme, whereas a positive identification of a neutrino mass below $\sim$ 0.1eV would clearly indicate a hierarchical mass scheme. [6] 19

2-1 KATRIN Experimental Setup. a) the WGTS, b) the transport system, c) the spectrometers, d) the beta detector. Printed from [6]. 25

2-2 The Windowless Gaseous Tritium Source (WGTS) and Pumping Sections. Printed from [6]. 28

2-3 The WGTS coordinate system used in this thesis. 30

3-1 Beta Decay Spectra and corresponding Kurie Plots for stationary (in the rest frame of the decay) T_2 decay for $m_\nu = 1$ and 0 eV/c^2. Note that, for $m_\nu = 0$, the Kurie plot is a straight line, whereas the Kurie plot for $m_\nu = 1$ eV/c^2 dips near the endpoint. This figure is constructed from the same stationary decay data sets as in Figs. 6.2.1-6.2.1. . . . 36

3-2 The distribution of final states of the $(^3HeT)^+$, constructed from Eq. 3.13 and the data given in 3.12. 39

5-1 Scaled Density/Pressure profile. This plot was constructed from the data from Ref. [10, 21] 49

6-1 Scaled z derivative of Pressure. This plot was constructed by using a spline interpolator tool with the data corresponding to Fig. 5.1 58

6-2 The flow velocity for tritium gas in the WGTS given by Eq. 5.28, evaluated at z = L/4, where L is the length of the WGTS. 58

6-3 A scatter plot of the distribution of particles within our 2D slice of the WGTS. 59

6-4 For a neutrino mass of $1\text{eV}/c^2$, the distortion of the beta spectrum, and corresponding Kurie plot, due to the influenced of thermal motion, flow velocity, and the final state distribution. These beta specra were constructed with $5 \cdot 10^9$ decay events. 60

6-5 For a neutrino mass of $0\text{eV}/c^2$, the distortion of the beta spectrum, and corresponding Kurie plot, due to the influenced of thermal motion, flow velocity, and the final state distribution. These beta specra were constructed with $5 \cdot 10^9$ decay events. 61

6-6 For a neutrino mass of $1\text{eV}/c^2$, the distortion of the beta spectrum, and corresponding Kurie plot, due to the influenced of thermal motion only. These beta specra were constructed via $7 \cdot 10^9$ decay events. . . 61

6-7 For a neutrino mass of $1\text{eV}/c^2$, the distortion of the beta spectrum, and corresponding Kurie plot, due to the influenced of the flow velocity only. Note that the scale of the energy axis of this figure is an order of magnitude less than the other figures considered in this section. These beta specra were constructed via $7 \cdot 10^9$ decay events. 62

6-8 For a neutrino mass of 1eV/c^2, the distortion of the beta spectrum, and corresponding Kurie plot, due to the influenced of both thermal motion and the flow velocity. This is the result of direct simulations of the two simultaneous effects, and was *not* obtained by simply adding Fig. 6.2.1 and Fig. 6.2.1. These beta specra were constructed via $7 \cdot 10^9$ decay events. 62

6-9 For a neutrino mass of 0.25eV/c^2, the distortion of the beta spectrum, and corresponding Kurie plot, due to the influenced of thermal motion only. These beta specra were constructed via $7 \cdot 10^9$ decay events. . . 63

6-10 For a neutrino mass of 0.25eV/c^2, the distortion of the beta spectrum, and corresponding Kurie plot, due to the influenced of the flow velocity only. Note that the scale of the energy axis of this figure is an order of magnitude less than the other figures considered in this section. These beta specra were constructed via $7 \cdot 10^9$ decay events. 63

6-11 For a neutrino mass of 0.25eV/c^2, the distortion of the beta spectrum, and corresponding Kurie plot, due to the influenced of both thermal motion and the flow velocity. Again, this is the result of direct simulations of the two simultaneous effects, and was *not* obtained by simply adding Fig. 6.2.1 and Fig. 6.2.1. These beta specra were constructed via $7 \cdot 10^9$ decay events. 64

6-12 For a neutrino mass of 0eV/c^2, the distortion of the beta spectrum, and corresponding Kurie plot, due to the influenced of thermal motion only. These beta specra were constructed via $7 \cdot 10^9$ decay events. . . 64

6-13 For a neutrino mass of 0eV/c^2, the distortion of the beta spectrum, and corresponding Kurie plot, due to the influenced of the flow velocity only. Note that the scale of the energy axis of this figure is an order of magnitude less than the other figures considered in this section. These beta specra were constructed via $7 \cdot 10^9$ decay events. 65

6-14 For a neutrino mass of $0\text{eV}/c^2$, the distortion of the beta spectrum, and corresponding Kurie plot, due to the influenced of both thermal motion and the flow velocity. Again, this is the result of direct simulations of the two simultaneous effects, and was *not* obtained by simply adding Fig. 6.2.1 and Fig. 6.2.1. These beta specra were constructed via $7 \cdot 10^9$ decay events. 65

6-15 The integrated spectra for a neutrino mass of $0.25\text{eV}/c^2$. This figure is simply given as a representative example of the spectra over the entire range that KATRIN will measure; the individual spectra are difficult to distinguish on this scale. 68

6-16 The integrated spectra for a neutrino mass of $1\text{eV}/c^2$. 69

6-17 The integrated spectra for a neutrino mass of $1\text{eV}/c^2$. 69

6-18 The integrated spectra for a neutrino mass of $1\text{eV}/\text{c}^2$. 70

Chapter 1

Massive Neutrinos

1.1 The Discovery of the Neutrino

In 1930, the understanding of nuclear beta decay was that a parent nucleus, P, decayed into a daughter nucleus, D, and an electron:

$$P \rightarrow D + e^{-} \tag{1.1}$$

This decay must obey both relativistic energy and momentum conservation laws, so for a given initial momentum of A, there are a total of two constraint equations on the momenta of the products, P and e^{-}. (Recall that energy is a function of momentum). Therefore, there are two unknowns (the momenta of P and e^{-}) and two constraint equations, so the system in completely determined and has no degrees of freedom. This means that, for a given initial momentum of A, there is one and only one allowed energy that the electron may possess. Thus, if we measure the electron energy spectrum (known as the beta spectrum) of Eq. 1.1 where A is at rest, we should find a single sharp peak at the energy determined by the conservation laws. Experiments, however, revealed a *continuous* beta spectrum (Fig. 1-1). If we believe that Eq. 1.1 truly describes the decay process, then this continuous spectrum, Fig. 1-1, violates energy/momentum conservation.[1, 2]

Many physicists, including Niels Bohr, were ready to interpret this as proof that

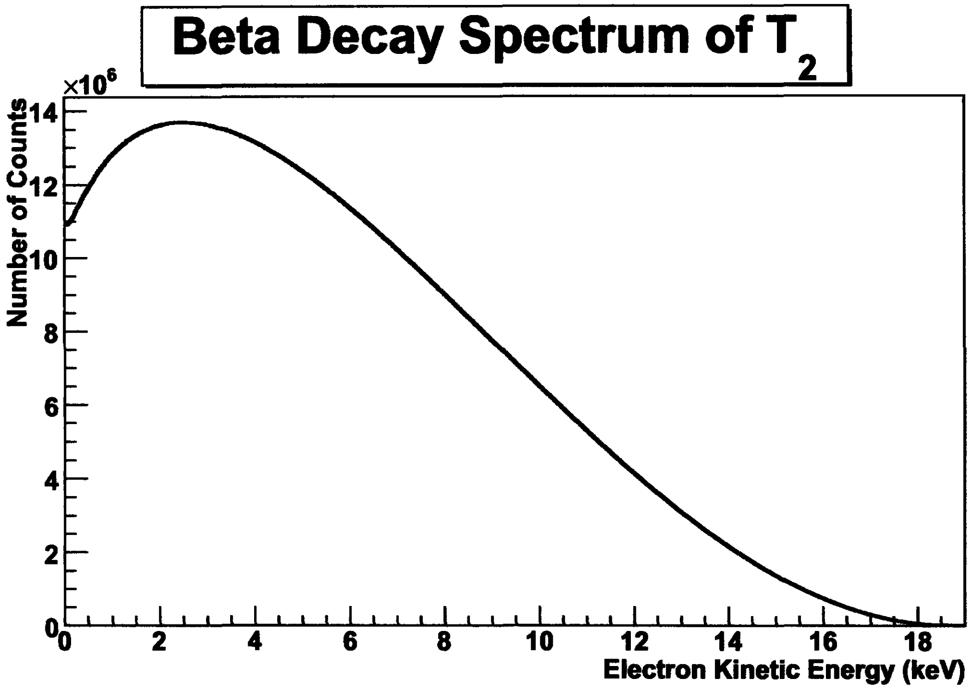

Figure 1-1: The Beta Decay Spectrum of molecular tritium, T_2. Note that this coninuous energy spectrum is inconsistent with momentum/energy conservation in a 2-body decay. This histogram was constructed from the stationary decay data in Fig. 6.2.1 and so, corresponds to a electron antineutrino mass of 1eV/c^2.

energy conservation was not actually a law of nature. Wolfgang Pauli, on the other hand, proposed that perhaps there was a third particle created in the decay. This would make the continuous energy spectrum possible, because it would introduce a third unknown (the momentum of this particle), giving the system an extra degree of freedom, so the electron energy would no longer be completely determined. This particle would have to be very light (perhaps massless) and carry no electric charge, to explain why it had not been observed. While it was greeted with skepticism at the time, this notion is now the standard model of beta decay, and the mysterious, elusive third particle is the electron antineutrino, $\bar{\nu}_e$.[1] The correct version of Eq. 1.1 is then

$$P \rightarrow D + e^- + \bar{\nu}_e \tag{1.2}$$

1.2 Motivation for a Non-Zero Neutrino Mass: Neutrino Oscillations

Neutrinos are created and interact via weak interactions, which is why they are so difficult to detect directly. There are three flavors of neutrinos that can participate in such reactions: the electron neutrino ν_e, the muon neutrino ν_μ, and the tau neutrino ν_τ. The Standard Solar Model, for example, predicts that the fusion reactions that take place in the Sun produce electron neutrinos. In the 1970's, the Homestake experiment, led by Dr. Raymond Davis, Jr., measured the flux of electron neutrinos received from the Sun and found this flux to be one third the flux predicted by the Standard Solar Model. Subsequent experiments designed to test these results also measured neutrino fluxes lower than the flux predicted by the Standard Solar Model.[3]

The question that naturally arises is whether the problem lies within the Standard Solar Model, the experiments themselves, or our understanding of neutrinos. Subsequent theoretic and experimental work isolates our understanding of neutrinos as the cause of this inconsistency. It was proposed that the flavor states, ν_3, ν_μ, ν_τ, discussed above, are not actually the energy eigenstates of neutrinos. These theories state that neutrinos are not actually massless particles, but instead may exist in a number of different mass eigenstates, and these mass eigenstates are the true energy eigenstates of the neutrino.[3, 4] Thus, for a mass eigenstate, $|\nu_j\rangle$, with energy eigenvalue E_j and mass eigenvalue m_j, we have

$$\hat{H}\,|\nu_j\rangle = E_j\,|\nu_j\rangle \tag{1.3}$$

In quantum mechanics, it is always possible to express a state as a superposition of energy eigenstates, so we can view a flavor eigenstate as a superposition of mass eigenstates.[5]

$$|\nu_f\rangle = \sum_j U_{fj}\,|\nu_j\rangle \tag{1.4}$$

Here, f denotes the flavor eigenstate, $f \in \{e, \mu, \tau\}$, and j again denotes the mass eigenstate, as in Eq. 1.3. The time evolution of a wavefunction is governed by Schrödinger's Equation. For a time-independent Hamiltonian, the Schrödinger Equation has the solution:[5]

$$|\psi(t)\rangle = e^{-\frac{i\hat{H}t}{\hbar}}\,|\psi(0)\rangle \tag{1.5}$$

Combining this together with Eq. 1.4 and 1.3, an expression for the time evolution of the wavefunction, $|\psi(t)\rangle$, of a neutrino that begins in a flavor eigenstate $|\nu_f\rangle$ is obtained:

$$|\psi(t)\rangle = e^{-\frac{i\hat{H}t}{\hbar}}\,|\nu_f\rangle = \sum_j U_{fj}e^{-\frac{iE_jt}{\hbar}}\,|\nu_j\rangle \tag{1.6}$$

Note that the exponential factor within the sum parameterizes the contribution of each mass eigenvalue to the neutrino's wavefunction at time t. These exponential factors can be represented as vectors rotating in the complex plane, like clock hands, each rotating at a rate determined by the energy E_j. Thus, these vectors are rotating at different rates, so their sum will vary as a function of time, changing the neutrino's wavefunction as a function of time. One can take the magnitude squared of the inner product of Eq. 1.6 with a different flavor eigenstate, $|\nu_g\rangle$, to calculate the probability that the neutrino be found in the flavor state $|\nu_g\rangle$ at time t. Due to this varying sum of the mass eigenvalues, this probability will change as a function of time. This means that the flavor of a neutrino is not constant in time, and a neutrino that is created in one flavor eigenstate may be found to be in another flavor eigenstate at a later time. This phenomenon is known as neutrino oscillations. [3, 4]

To summarize, when neutrinos participate in weak interactions, they do so in a flavor eigenstate. This means that neutrinos are created in a flavor eigenstate and are detected in flavor eigenstates. However, since these flavor states are not also energy eigenstates, a neutrino's wavefunction changes in time between different mixtures of these flavor eigenstates. This means that a neutrino created as an electron neutrino in the Sun may be detected as a different flavor of neutrino on Earth, due to these flavor mixing oscillations on its journey. Neutrino oscillations could thereby explain the experimental observations; reduced fluxes were observed simply because the experiments were not detecting all three flavors of neutrinos.

A number of experiments have been performed to test this neutrino oscillation theory by detecting the different flavors of neutrinos. The first of these experiments to definitively verify neutrino oscillations, and thereby save the Standard Solar Model, was the Sudbury Neutrino Observatory (SNO) experiment. This experiment measured the fluxes of all three flavors, reconstructing a total flux that is consistent with the flux predicted by the Standard Solar Model. The results also agreed with neutrino oscillation models that consider the effects of the passage of neutrinos through matter, which the simplified version presented above does not.[3]

These neutrino oscillation experiments, however, only measure the *differences* of the squared neutrino masses and cannot measure scales of the actual neutrino masses themselves. This mass difference arises from Taylor expanding the relativistic expression for energy, $E_j = \sqrt{p_\nu^2 + m_j^2} \approx p_\nu + \frac{m_j^2}{2p_\nu}$, under the assumption that the momentum of the neutrino is much larger than any of the mass eigenvalues. When taking the inner product with Eq. 1.6 to calculate probabilities, plugging in this approximated energy expression yields a term that is the difference between the squared mass eigenvalues, [4]

$$\Delta m_{jk}^2 \equiv \left| m_j^2 - m_k^2 \right| \tag{1.7}$$

Since they are only sensitive to this mass difference, oscillation experiments shed no light on issues such as, whether the neutrino masses are hierarchical or nearly degenerate, for example (see next section). Despite this limitation, the oscillation experiments are not completely silent on the question of the absolute neutrino mass scale; it is known that the inequality

$$(m_j \text{ } or \text{ } m_k) \geq \sqrt{\left|\Delta m_{jk}^2\right|} \tag{1.8}$$

should be satisfied by at least one neutrino mass eigenvalue. [6] Therefore neutrino oscillation experiments can give a *lower* bound on the scale of the neutrino mass. The results of Super-Kamiokande's analysis of atmospheric neutrinos gives a lower bound of (0.04 - 0.07) eV [6].

1.3 The Impact of the Neutrino Mass Scale

So, these neutrino oscillation experiments have confirmed (with a no-oscillation probability of 0.5%) neutrino oscillations, and in so doing, confirmed that neutrinos do not have zero mass, as predicted by the Standard Model.[6] Now that all this is established, what motivation have we for measuring the absolute scale of these neutrino masses? Is it only to neatly round out a textbook chapter on neutrinos with a nice little chart of neutrino masses? The answer, of course, is that there are still many open questions upon which the absolute neutrino mass can shed light. In fact, there are too many to list here in full detail, so we will only examine a handful, superficially.

As one would expect, this observed violation of the Standard Model has motivated the birth of many new theories that extend beyond the Standard Model to explain the origin of this non-zero neutrino mass. These theories generally fall into one of two categories: a *hierarchical* neutrino mass scheme ($m1 \ll m2 \ll m3$), or a nearly *degenerate* neutrino mass scheme ($m1 \approx m2 \approx m3$).[6] Figure 1-2 demonstrates the dependencies of these two scenarios on the absolute scale of the neutrino mass. As shown, the dividing line between these two theories is a neutrino mass scale of

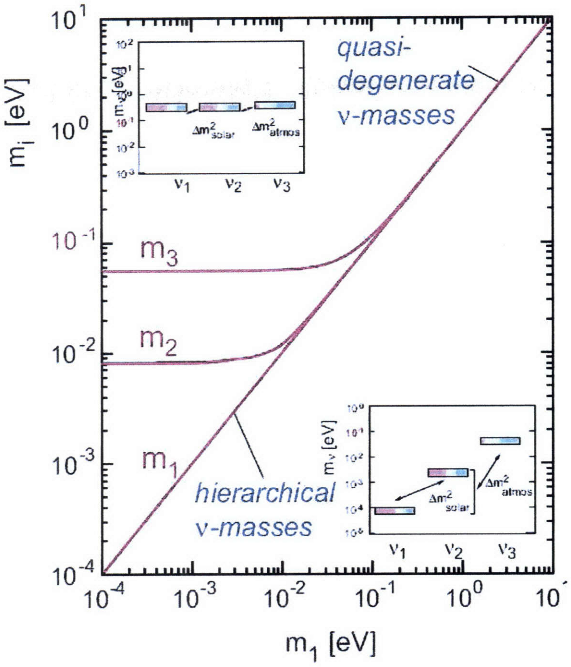

Figure 1-2: The impact of the neutrino mass scale on the question of hierarchical or degenerate neutrino masses. Plotted are the neutrino mass eigenvalues (m1<m2<m3) as a function of the value of the lightest eigenvalue, m1. One can see that a positive identification of a neutrino mass *above* ~ 0.1eV would clearly indicate a quasi-degenerate mass scheme, whereas a positive identification of a neutrino mass below ~ 0.1eV would clearly indicate a hierarchical mass scheme. [6]

~ 0.1eV.

Another general division between theoretical models of neutrinos concerns the relationship between neutrinos and their anti-particles. Some models predict that a neutrino is its own antiparticle; these types of neutrinos are called Majorana type neutrinos. Others say that the neutrino and its antiparticle are actually distinct particles with different lepton numbers; these types of neutrinos are called Dirac type neutrinos. [6]

An example of a group of theories that make distinctions between such details are "Seesaw" models. These models are designed to explain the masses of Majorana type neutrinos. The Seesaw I mechanism predicts a hierarchical mass scheme and calls for heavy right-handed neutrinos in addition to light left-handed neutrinos. The name, "seesaw", arises due to the fact that, the lighter the left-handed neutrinos are, the heavier the right-handed ones will be. The Seesaw II mechanism, however, calls for the quasi-degenerate mass scheme and a Higgs triplet to which the neutrinos are coupled. [6]

The scale of the neutrino mass is also an important parameter in cosmology. As pointed out in Refs. [6], [7], cosmological models are currently plagued by "parameter degeneracy." This means that experimental results can be adequately explained by different sets of combinations of cosmological parameters. In other words, the data cannot distinguish between many possible descriptions of the Universe. Since the neutrino mass enters into these sets of cosmological parameters, knowledge of the neutrino mass could help lift some of this degeneracy by eliminating the neutrino mass as a floating unknown parameter in these fits.

The neutrino mass is also important in determining the relationship between neutrinos and dark matter. As quoted in Ref. [8], the Tremaine-Gunn bound claims that, for neutrinos to make up the dark matter in the Milky Way Galaxy, they would have to be larger than about 25eV. The results of the Mainz and Troitsk experiments therefore already rule out the possibility that Standard Model neutrinos make up the dominant fraction of dark matter. However, the specific role of neutrino hot dark matter on the formation of large scale structures is still to be determined, and is very closely related to the total neutrino density of the universe Ω_ν.

Hannestad [8, 7] also discusses the possible relationship between cosmic rays and neutrinos. In the Z-burst model of cosmic rays, neutrinos annihilate with other neutrinos in the cosmic background, producing protons. In order for ultra high energy cosmic rays to be explained by this Z-burst model, a neutrino mass of $0.26^{+0.20}_{-0.14}$eV is required.

Chapter 2

The KATRIN Experiment

As discussed in the previous section, the absolute scale of the neutrino mass has many implications in particle and astrophysics. A great deal of the implications lie in distinguishing between competing theories. Therefore, if one were to determine the scale of the neutrino mass in a way that is independent of such theories (a so-called "model-independent determination"), then the result would have twofold advantages over model-dependent determinations. First, one could argue that the model-independent determination would be more satisfy or convincing, for it is not based on a controversial new theory. Second, and most importantly, a model-independent determination could help place a constraint on these new theories and help determine which may be correct and which cannot be correct. The fact that the neutrino has a non-zero mass points to new physics beyond the Standard Model, and a model-independent determination of that mass can help us understand what this new physics may be.

2.1 The Theory

Nuclear beta decay is a process whereby a parent nucleus decays into a daughter nucleus, an electron, e^-, and an electron antineutrino $\bar{\nu}_e$. The relevant details of the beta decay considered in the KATRIN experiment will be discussed in more detail in Chapter 3. For now we are interested only in the fact that beta decay produces an electron with an energy spectrum with a shape described by:

$$\frac{d^2N}{dtdE} = KF(E,Z)p(E+m_ec^2)(E_0-E)\sqrt{(E_0-E)^2-m_\nu^2c^4} \tag{2.1}$$

Here, E is the kinetic energy of the electron, while p and m_e and are the momentum and rest mass of the electron. m_ν^2 is the neutrino mass observable, K is the matrix element associated with the decay, and E_0 is the endpoint energy. $\frac{d^2N}{dtdE}$ is the count rate of electrons within an energy width of dE.[9]

Since the neutrino mass appears in this expression, the value of the neutrino mass affects the shape of this electron energy spectrum. Since the other parameters in this equation are known, a careful examination of the energy spectrum of electrons produced in beta decay would reveal the value of this neutrino mass observable. Furthermore, determining the neutrino mass in this fashion would be classified as model-independent, because it is based on the generally non-controversial and accepted theory of nuclear beta decay. This, in a nutshell, is how KATRIN aims to glean the neutrino mass, by examining the electron energy spectrum in nuclear beta decay.[6]

A closer examination of Eq. 2.1 reveals that the effect of the neutrino mass is most prominent when the electron energy is near the endpoint energy, E_0. However, as the electron energy approaches this high energy region, the count rate (Eq. 2.1) correspondingly drops very quickly. Therefore, the fraction of electrons produced which are relevant to the neutrino mass determination is extremely small. This fact imposes special constraints on experimental design. Maximizing the count rate of electrons in this endpoint region is crucial to the success of an experiment of this type.

As will be discussed in the beta decay chapter, one way to maximize the relevant count rate is to examine the beta decay of an isotope with a low endpoint. ^{187}Re, with an endpoint of 2.5keV, and ^3H (also known as "tritium" and denoted as T), with an endpoint of 18.6keV, are the two isotopes with the lowest known endpoints in nature, so they are the prime candidates for such an experiment. Even though tritium possesses the higher of these two endpoints, it also possesses additional qualities that make it the more attractive candidate for experiment. First of all, tritium has a half-life of 12.3 years compared to the ^{187}Re half life of $4.5 \cdot 10^{10}$ years, which greatly increases the count rate. Also, tritium is the simpler of the two isotopes; the structures of the atoms and molecules involved in the beta decay of tritium are simpler than those for ^{187}Re. This is an advantage because calculations involving the final states of these molecules in the decay and scattering with these molecules must be included in the analysis of spectrometer experiments. Another advantage of tritium is that the beta decay is super-allowed, which means that the matrix elements involved in Eq. 2.1 is relatively simple. Therefore, using tritium as a source for beta decay provides the most favorable balance of count rate and computational simplicity for a spectrometer experiment.

2.2 The Status of Neutrino Mass Determination

This idea of examining the beta decay spectrum of tritium to determine the neutrino mass is not what is new about KATRIN. There have been other such beta decay experiments, two of which will be discussed here. An experiment in Mainz, Germany and one in Troitsk, Russia both examined the beta spectrum of tritium using MAC-E filter type spectrometers (see Section 2.4.1). However, the Troitsk experiment used a windowless gaseous tritium source while the Mainz tritium source was a thin film of molecular tritium quench-condensed onto a graphite substrate (at temperatures below 2K).[6]

At first, the Troitsk group observed an anomaly that resembled a step in the count rate a few eV below the endpoint energy. After reducing background and comparing measurements to those taken at Mainz, it was decided that this anomaly was merely an experimental artifact. Assuming that this effect was, in fact, an anomaly, the Troitsk group's analysis of data taken 1994-2001 yields a bound on the electron antineutrino mass of[6]

$$m_\nu^2 = (-2.3 \pm 2.5 \pm 2.0)\frac{eV^2}{c^4}; m_\nu < 2.05\frac{eV}{c^2}(95\% C.L.) \tag{2.2}$$

Analysis of the Mainz data from the years 1998, 1999, and 2001 yield a bound of[6]

$$m_\nu^2 = (-0.6 \pm 2.2 \pm 2.1)\frac{eV^2}{c^4}; m_\nu < 2.3\frac{eV}{c^2}(95\% C.L.) \tag{2.3}$$

Thus, the current upper bound on the electron antineutrino mass is about 2eV/c^2. The KATRIN experiment is designed to reduce this bound by an order of magnitude by yielding a mass sensitivity of 0.2eV/c^2.

2.3 Advantages of KATRIN

In the previous section, various implication and questions surrounding the absolute scale of the neutrino mass were discussed. The natural question that arises is, "What impact will the results of the KATRIN experiment have on these questions?" To revisit the list, on the topic of hierarchical vs. quasi-degenerate mass schemes, the sensitivity of KATRIN lies on the dividing line between these two schemes. If the result of KATRIN is a positive mass identification, then this will fall in the region of quasi-degenerate masses. If KATRIN results in no positive mass identification and only an upper bound, then its sensitivity is such that this bound will rule out the quasi-degenerate mass scheme, implying a hierarchical scheme. Thus, KATRIN will be able to settle the debate between hierarchical and quasi-degenerate mass schemes. This will, for instance, help weed out certain Seesaw theories.[6]

KATRIN makes no assumptions as to whether neutrinos are of the Majorana or Dirac type, so KATRIN's mass determination therefore holds independent of which of these models, if either, is true. Similarly, impact of KATRIN's results on cosmology largely relies on the fact that this result will be a "direct," or model-independent, measurement of the neutrino mass. Thus, KATRIN's results will lead to either fully determined or at least more constrained input parameters for the various cosmolog-

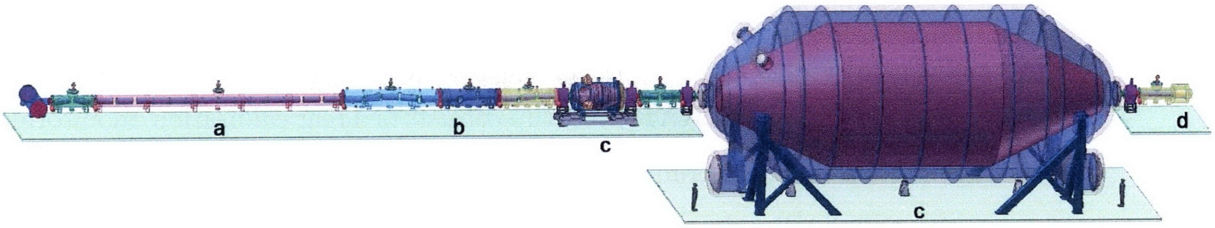

Figure 2-1: KATRIN Experimental Setup. a) the WGTS, b) the transport system, c) the spectrometers, d) the beta detector. Printed from [6].

ical models. This will help alleviate the problem of parameter degeneracy. Also, if KATRIN results in a positive identification of a neutrino mass (and not just an upper bound), this will determine the neutrino hot dark matter contribution to the matter density. KATRIN may also demonstrate definitively that primordial neutrinos do not contribute substantially to the Universe mass and energy densities. With respect to astrophysics, the KATRIN results could test the Z-burst model described in the previous chapter.[6]

2.4 The KATRIN Setup

The Karlsruhe Tritium Neutrino (KATRIN) experiment, located in Karlsruhe, Germany, is designed to measure the neutrino mass, via examining the beta decay of tritium, to a sensitivity of $0.2\text{eV}/c^2$. The considerations of this thesis deal mostly with the tritium source (WGTS), so the WGTS will necessarily be discussed here in more technical detail. However, it is difficult to understand the function and purpose of just one piece of a machine in isolation. Therefore, we will also briefly examine the other components of the KATRIN experiment to give a sense of the scale and interplay between these parts. These components would be of great importance if one were to extend my simulation to include the passage of electrons through the entire apparatus. [6]

2.4.1 Experimental Overview

As can be seen in Fig. 2-1, the KATRIN setup consists of a rear calibration/monitoring section, the tritium source, a transport/pumping section, a pre-spectrometer, a main spectrometer, and, finally, the electron detector. The rear section, Control and Monitor Section (CMS), will house electron guns and detectors. The electron guns will be used to investigate the transmission of electrons through the KATRIN apparatus. In this way a response function can be determined, characterizing the energy losses of electrons, which can be used for calibration and the determination of systematic uncertainties. Detectors will also be placed in this system to monitor the activity of the source. [6]

After the rear section is the Windowless Gaseous Tritium Source (WGTS), which maintains a high density of high purity tritium gas. It is this tritium that undergoes beta decay to produce the electrons that will be measured. To maintain a high level of pure tritium in this source, the tritium gas is pumped in a closed loop system. The WGTS is described in greater detail in the next section. [6]

Electrons created in the WGTS are guided through the transport system to the spectrometers. However, tritium can also travel out of the WGTS and find its way to the spectrometers. Tritium inside the spectrometers would result in an undesirable background rate, so the amount of tritium that enters the spectrometers must be severely limited. The pumps within the WGTS already reduce the tritium flow by a factor of 10^3, but further reduction is necessary, and this is the job of the transport system. The first section of the transport system consists of another differential pumping system to pump the tritium out of the transport system. The portions of this pumping system that are adjacent to the WGTS are matched up carefully with the conditions (magnetic field and temperature) within the WGTS to ensure stable operating conditions of the WGTS. After the pumping systems have significantly reduced the tritium flow, a passive cryotrapping system, maintained at a temperature of 4.5K, absorbs much of the remainder of the tritium. All together, the transport system reduces the tritium flow rate, between the WGTS output and the pre-spectrometer entrance, by a total factor of about 10^{11}. This results in a background count rate, due to tritium decay inside the spectrometers, of less than 10^{-3} counts per second. In addition to these pumps downstream of the WGTS, there is also a set of pumps between the WGTS and the rear system. These pumps help prevent tritium from entering the rear system and, more important to this thesis, make the pressure profile within the WGTS symmetric about the injection point. Besides reducing the flow of tritium to the spectrometers, the transport system also adiabatically guides the electrons towards the pre-spectrometer. [6]

After the transport system is the pre-spectrometer, followed by the main spectrometer. The spectrometers are MAC-E Filters (Magnetic Adiabatic Collimation combined with an Electrostatic Filter), which act as integrating high-energy pass filters. In such filters, the electrons emitted from the source, with isotropic directionality, are channeled into a beam by the use of magnetic fields. (In this broad beam, the electron velocities are nearly parallel to the magnetic field lines). This beam of electrons then passes through an electrostatic retarding potential. Electrons without a high enough energy to overcome this potential are reflected back, while electrons with energies above the retarding threshold are transmitted and then re-accelerated and collimated via magnetic fields. Thus, only electrons with energy above a certain threshold (set by the retarding potential) are transmitted through the spectrometer. [6]

The KATRIN spectrometers have the additional design feature that the retarding high voltage is connected directly to the hull of the spectrometer. Inside the spectrometer, attached at a distance all along the inner surface of the spectrometer, are sets of thin wire electrodes that are maintained at a potential slightly more negative than that of the hull. This acts to suppress low-energy electrons that are ejected from the hull walls and to prevent the formation of Penning traps near the corners of the hull. [6]

The pre-spectrometer filters out all electrons with energies below 18.3keV. As discussed above, only the high-energy portion of the electron spectrum near the endpoint contains information about the neutrino mass. By filtering out these unnecessary elec-

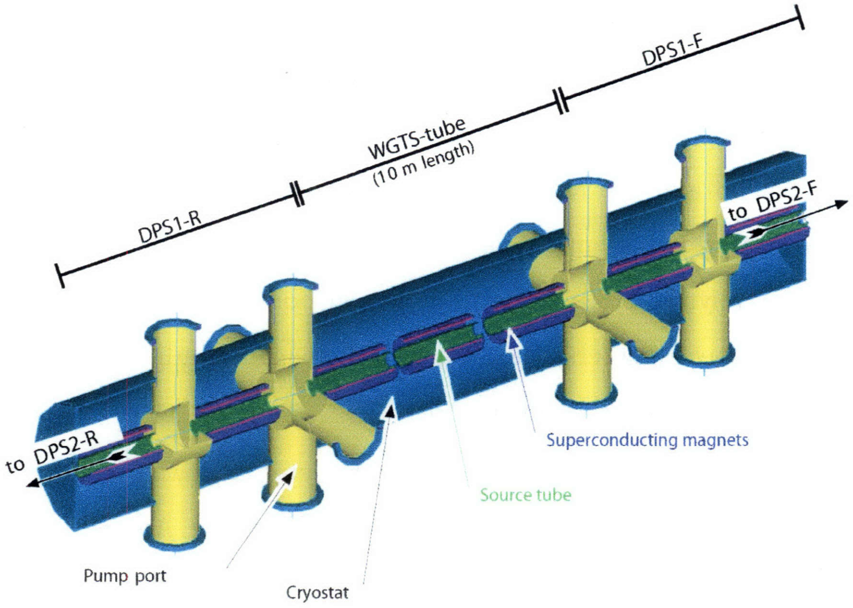

Figure 2-2: The Windowless Gaseous Tritium Source (WGTS) and Pumping Sections. Printed from [6].

trons before the main spectrometer, a background due to ionization of residual gas in the main spectrometer is reduced. The remaining high-energy electrons then pass through a 2m transport system of two superconducting solenoids and then into the main spectrometer. This spectrometer measures this last approximately 300eV of the beta spectrum with an energy resolution of 0.93eV. The rate of electrons entering into the main spectrometer will be approximately 10^3 per second.[9] The pre-spectrometer has an outer diameter of 1.7m and is 3.38m long. The main spectrometer has an outer diameter of 10m and a length of 23m. Both spectrometers are maintained at a pressure of less than 10^{-11}mbar. [6]

The electrons that leave the main spectrometer will then travel through another short transport system and finally impinge upon a multi-pixel, ultra-high energy resolution silicon semiconductor detector. In this way, the energy spectrum of the electrons created via beta decay in the WGTS can be examined by dialing the retarding voltage of the spectrometer. [6]

2.4.2 The WGTS in Detail

As discussed, a very small fraction of the beta spectrum is relevant to the determination of the neutrino mass, so a very high count rate of beta decays is needed to obtain the statistics necessary for experimental observation. This high decay rate is accomplished in the WGTS, which yields a beta decay rate of approximately 10^{11} decays per second. The WGTS consists of a tube, 10m long and 90mm in diameter. Molecular tritium gas, T_2, maintained at a high isotopic purity of greater than 95%, monitored by Raman spectroscopy, is injected into the center of the WGTS through over 250 holes of 2mm diameter (to avoid gas jets) at a rate of 40g/day (with stability level 0.1%). From the injection point, the tritium travels the length of 5m via diffusion to either end of the tube, spending a time of $\sim 1s$ in the WGTS. As a result, each single tritium molecule has a probability of about 10^{-9} to decay within the WGTS. [6]

The tritium within the WGTS is maintained at a temperature of 27K with a stability to 0.1%. A low temperature is desirable because it decreases the random thermal motion of the tritium and allows this high density of tritium to be maintained at a relatively low pressure, and so, relatively low flow rate. This is important because it helps to reduce the Doppler broadening of the spectrometer measurements, which is the topic of this thesis. A temperature much lower than this, while it would further reduce this Doppler broadening, is not possible. This is due to the fact that, at lower temperatures, the tritium molecules may begin to cluster together. Since these clusters have different final electronic states than the molecular tritium, their formation would introduce new and uncontrollable statistical uncertainties. Therefore, the Doppler broadening at 27K represents the optimal balance between statistical uncertainties and cannot be removed by lowering the temperature further. [6]

The WGTS in encircled by superconducting solenoids that maintain the entire source at a magnetic field of 3.6T. This magnetic field serves to adiabatically guide the electrons produced in the source by beta decay to the ends of the WGTS. To maintain the high tritium concentration within the WGTS, the tritium is circulated within a nearly closed loop. This is accomplished by a differential pumping system of

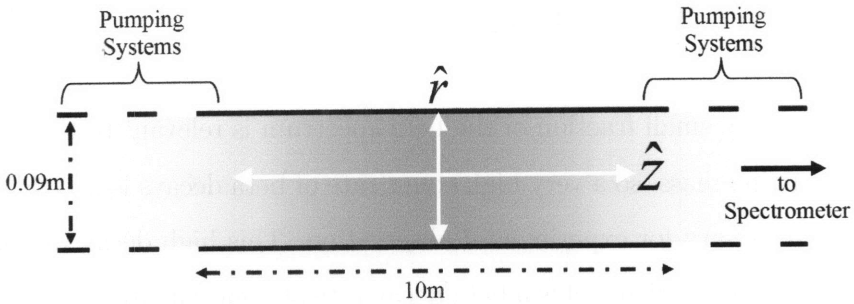

Figure 2-3: The WGTS coordinate system used in this thesis.

turbomolecular pumps located on either end of the WGTS. This differential pumping leads to a density/pressure profile within the WGTS that will be discussed in detail later. [6]

In our analysis, we will assume that the WGTS is axially symmetric, and thus, analysis of the system can be reduced to a two-dimensional analysis (we partially lift the one-dimensional assumption in Ref. [10]). Let us establish the coordinate system that z is the coordinate along the axis of the WGTS, and that the positive z direction points toward the main spectrometer. The other relevant coordinate is then r, the radial distance from the axis of the WGTS. Because of the rotational symmetry about the axis, we will consider only a two-dimensional plane described by r and z.

Chapter 3

Beta Decay

3.1 Fermi's Golden Rule

Fermi's Golden Rule is the rule that governs the transition rate of a system into a continuum of states. It can be derived, in quantum mechanics, from time-dependent perturbation theory, where the time-dependent Hamiltonian is expanded into a time-dependent and a time-independent portion:[5]

$$H(t) = H^0 + H^1(t) \tag{3.1}$$

And $H^1(t)$ is assumed to be expressible in the form

$$H^1(t) = H^1 e^{-i\omega t} \tag{3.2}$$

The final result is

$$R_{i \to f} = \frac{2\pi}{\hbar} \left| \left\langle f^0 \middle| H^1 \middle| i^0 \right\rangle \right|^2 \delta(E_f^0 - E_i^0 - \hbar\omega) \tag{3.3}$$

$R_{i \to f}$ is the transition rate from state i to state f, and the superscripts denote to what order of the Hamiltonian the quantities correspond. This equation applies to many systems that undergo transitions, including nuclear decay. [5]

3.2 Tritium Beta Decay

Nuclear decays are governed by Fermi's Golden Rule (Eq. 3.3), where the "transition" that occurs is the actual decay, where the parent nucleus decays into a daughter nucleus and possibly various other products. For nuclear decays, the golden rule separates into a matrix element and a phase-space factor. [1] The matrix element encodes the dynamical information about the decay, and the phase-space factor describes the kinematic information. Loosely speaking, the phase-space factor adds a weighting based on the relative number of different possible states and configurations available in a decay. One can think of the phase-space factor as characterizing the number of ways one can distribute the available energy of the decay among the momenta of the various products. The beta decay of the neutron has a relatively small amount of phase space available due to the relatively small difference between the rest energy of the parent and the sum of the rest energies of the products. This difference in rest energies, by relativistic energy conservation, is equal to the total kinetic energy available to the products in the decay, and is referred to as the decay's *endpoint*, (mentioned earlier) and is denoted by E_0. Since the phase-space element describes the possible ways to distribute this kinetic energy between the particles (while conserving momentum), the small size of this kinetic energy is a constraint that translates into a smaller phase-space factor. This is why the rest masses of the products have such a significant effect on the shape of the energy spectra in neutron beta decay; the rest-energies of the electron and perhaps the neutrino are non-negligible fractions of the total energy released in the decay. This is a reason why the low endpoint of tritium is so attractive in performing neutrino mass experiments that examine the shape of the beta spectrum. In decays with larger phase-space factors, one may be able to neglect the rest energies of certain products. [1] The beta decay of atomic tritium (^3H, or T) is described by the equation:

$$T \rightarrow^3 He^+ + e^- + \bar{\nu_e} \tag{3.4}$$

So, for the specific case of atomic tritium decay, Fermi's Golden Rule takes the form: [1]

$$d\Gamma = \frac{\langle |M|^2 \rangle}{2\hbar m_T} \left(\frac{c d^3 \vec{p_\nu}}{(2\pi)^3 2E_\nu} \right) \left(\frac{c d^3 \vec{p_{He+}}}{(2\pi)^3 2E_{He+}} \right) \left(\frac{c d^3 \vec{p_e}}{(2\pi)^3 2E_e} \right) (2\pi)^4 \delta^4 (p_T - p_\nu - p_{He+} - p_e) \tag{3.5}$$

Here, the subscript He+ denotes the $^3He^+$ daughter. The matrix element can be evaluated various ways. Ref. [1] expands the matrix element by using Feynman diagrams, while Ref. [11] performs a full relativistic treatment by expanding the matrix element in a sort of a Taylor series. The relativistic argument is that $|M|^2$ is a Lorentz invariant term, and so, can be expanded as a sum over Lorentz invariant quantities. The most general form, up to two powers of momenta is then[11]

$$|M|^2 = A - B\vec{p_e} \cdot \vec{p_\nu} - C\vec{p_{He+}} \cdot \vec{p_{initial}} + \ldots \tag{3.6}$$

In general, A, B, and C are arbitrary constants, but Ref [11] argues that, for the tritium decay, $A = C = 0$, and $B \neq 0$. Thus, combining Eq. 3.5 and Eq. 3.6, the total weighting factor for a given set of four-momenta of the three products is simply the phase-space factor multiplied by the dot product of the four-momenta of the electron and the neutrino. This is relevant to the simulations performed for this thesis, because the simulation package that is used produces four-momenta of products weighted solely by the phase-space factor. In order to transform these results into products specifically of tritium beta decay, this extra dot-product weighting is added. Eq. 3.5 and Eq. 3.6 can further be manipulated algebraically, momenta can be integrated over, and a final Fermi correction (see next section) can be added to produce the final electron energy spectrum given in Eq. 2.1.[2, 1, 11]

3.3 The Fermi Function

The above considerations, however, do not take electromagnetic forces into account. The electron that is being ejected carries a negative charge, and, as a result of loosing this electron, the daughter nucleus has a net positive charge. Therefore, we expect

Coulombic forces between these two charged products to affect the kinematics described above. Since the force is attractive, the actual speed of the electron (and so, its energy) is smaller than that predicted purely by kinematics. Because the full derivation of the Fermi function is beyond the scope of this thesis, let us try to understand the effect and its dependencies qualitatively. First, we expect this effect to depend upon the charge of the daughter nucleus, Z, because this will affect the overall strength of the Coulombic force. Second, electrons ejected with low energies move at slower speeds than electrons ejected with higher energies. Consequently, lower energy electrons spend more time close to the daughter nucleus (i.e. in regions of strongest Coulombic attraction) than higher energy electrons. Therefore, the effect of Coulombic interactions will be larger for low energy electrons, so we expect this Coulombic effect to also be a function of the electron energy. This energy-dependent Coulombic effect therefore changes the weighting of electron energies in our spectrum, and its distortion should be largest in the lower energy region. We can characterize this effect then by multiplying the energy spectrum by a correction factor, F(Z, E). This factor, F(Z, E) is known as the Fermi function, and is quite complicated. However, in the non-relativistic limit, it can be approximated as[2]

$$F(Z,E) = x\left(1 - e^{-x}\right)^{-1} \tag{3.7}$$

Where

$$x = \frac{2\pi Z\alpha}{\beta} \tag{3.8}$$

Where α is the fine structure constant, E is the total energy of the electron, and β is the velocity of the electron divided by c. An improved version of this approximation is presented by Ref. [12]

$$F(Z,E) = x\left(1 - e^{-x}\right)^{-1}[a_0 + a_1\beta] \tag{3.9}$$

Here, the constants a_0 and a_1 are determined empirically to be $a_0 = 1.002037$ and $a_1 = -0.001427$. Eq. 3.9 agrees with the relativistic calculations of Ref. [13] over the energy range involved in the determination of the neutrino mass. Thus, this is the expression for the Fermi function that is used in the calculations in this thesis.

3.4 The Kurie Plot

The effect of the neutrino mass upon the beta spectrum is not very visibly apparent unless different spectra corresponding to different neutrino masses are superimposed. An alternative representation of the beta spectrum, called the Kurie plot, makes the effect of a non-zero neutrino mass quite vivid. When comparing different beta spectra, Kurie plots are often used, due to their relatively simple, mostly linear nature.[2]

The beta energy spectrum, Eq. 2.1, reduces to the following expression in the case of a zero neutrino mass:

$$\frac{d^2N}{dtdE} = KF(E,Z)p(E_{tot})(E_0 - E)^2 \tag{3.10}$$

where E_{tot} is the total energy of the electron $(E + m_e c^2)$. If we define $N(E)$ to be the number of electrons with kinetic energy within a range of $[E,\ E + dE]$ in a time interval dt, then we can rearrange Eq. 3.10 as follows

$$\left[\frac{N(E)}{pE_{tot}F(E,Z)}\right]^{1/2} = C(E_0 - E) \tag{3.11}$$

Thus, if we plot the quantity $\sqrt{\frac{N(E)}{pE_{tot}F(E,Z)}}$ against the electron energy, the plot will be linear (for the case of zero neutrino mass) and will intercept the E-axis at the endpoint energy, E_0.[2, 9] However, due to the difference between Eq. 2.1 and Eq. 3.10, the Kurie plot for a beta spectrum corresponding to a non-zero neutrino mass will be mostly linear but will contain a slight dip near the endpoint. (See Fig. 3.4).

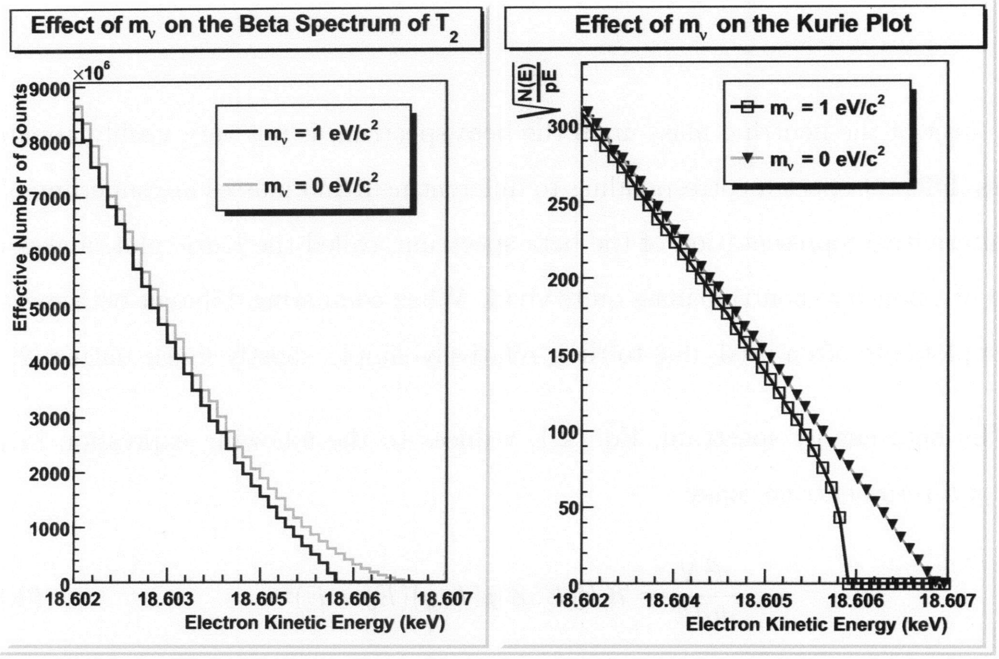

Figure 3-1: Beta Decay Spectra and corresponding Kurie Plots for stationary (in the rest frame of the decay) T_2 decay for $m_\nu = 1$ and 0 eV/c^2. Note that, for $m_\nu = 0$, the Kurie plot is a straight line, whereas the Kurie plot for $m_\nu = 1$ eV/c^2 dips near the endpoint. This figure is constructed from the same stationary decay data sets as in Figs. 6.2.1-6.2.1.

3.5 Molecular Decay and Final State Distribution

The tritium source that will be producing the beta decays in the KATRIN experiment is tritium gas. This tritium gas consists primarily of tritium *molecules*, T_2. This *molecular* tritium gas is inherently more complicated than the pure, *atomic* tritium considered in Eq. 2.1. Molecules can possess certain vibrational and rotational states that pure atoms do not. For instance, if we consider a classical toy model of a diatomic molecule, such as T_2, we model the molecule as two hard spheres (the atoms) connected by a spring (the bond between the atoms). Let us consider the states of a molecule at rest in this model. One state consists of the two spheres remaining at rest with respect to one another, with the spring remaining at its rest length. This is analogous to the state of just one single sphere. However, the spheres may also oscillate towards and away from each other symmetrically about the center of the spring. This latter state has a higher energy associated with it than the former, however in both cases, the molecule is at rest, so this energy is not associated with the motion of the molecule's center of mass. Thus, this second state possess a certain *internal* energy, due to the vibrations of the constituent atoms. A single hard sphere does not possess such a *vibrational* state. Furthermore, rotations of the "molecule" about different axes now have different energies because the molecule is not spherically symmetric, as the atom is. Of course the true rotational and vibrational states of a molecule is much more complicated and is governed by quantum mechanics, but this model serves to lend an intuitive picture to the notion of vibrational and rotational states.[14, 15] The decay of molecular tritium ($^3H_2$, or T_2) is described by[6]

$$T_2 \rightarrow (^3HeT)^+ + e^- + \bar{\nu}_e \tag{3.12}$$

Since the $(^3HeT)^+$ ion is a molecule, it can exist in a number of rotational-vibrational states. Thus, when T_2 decays, a certain amount of the energy released by the decay goes into exciting a rotational-vibrational state of the $(^3HeT)^+$ ion. We will henceforth refer to the state of the $(^3HeT)^+$ ion in Eq. 3.12 as the "final state." Energy conservation then dictates that the total kinetic energy of the decay (the endpoint) is decreased by an amount equal to this final state energy. Thus, the endpoint of the molecular tritium decay, Eq. 3.12, is actually a function of the final state of the $(^3HeT)^+$ molecular ion. The distribution of these final states therefore influences the shape of the observed beta spectrum near the endpoint. Since the determination of the neutrino mass is dependent upon this very shape, simulations of the tritium decay in KATRIN must include this final state distribution in order to be accurate. In addition to the rotational-vibrational states mentioned above, the daughter $(^3HeT)^+$ could also exist in a number of electronic excited states, which would also affect this final state distribution. However, analysis has shown that these excited states are negligible compared to these rotational-vibrational states. [6] Therefore a distribution of final states due to rotational-vibrational states is sufficient for the purposes of KATRIN. The distribution of such states is, again, determined by Fermi's Golden Rule, Eq. 3.3. Here, the two wavefunctions considered are that of the parent T_2 and that of the daughter $(^3HeT)^+$. The H^1 is an expression that includes the recoil of the emitted electron. From this starting point, simulations are performed under the sudden approximation to produce the final state distribution. The sudden approximation is the assumption that the interaction between the electron and the $(^3HeT)^+$ ion is negligible.[15] The distribution produced consists of a discrete, low-energy distribution, and a high-energy tail. The tail is described by[14]

$$P(E) \simeq 14.7 \left(\frac{8e^{-4arctan(\kappa)/\kappa}}{\sqrt{1-e^{-4\pi}}(1+\kappa^2)^2} \right)^2 \frac{dE}{eV} \tag{3.13}$$

where the probability P(E) is given as a percent, and $\kappa = \sqrt{(E - 45eV)/13.606eV}$.

For the purposes of my simulation, I discretized the tail in intervals of 0.1eV, to match the smallest resolution given for the discrete portion, and combined both together into a histogram (Fig. 3.5). The final state energies thrown from this histogram were added to the rest mass of the $(^3HeT)^+$.

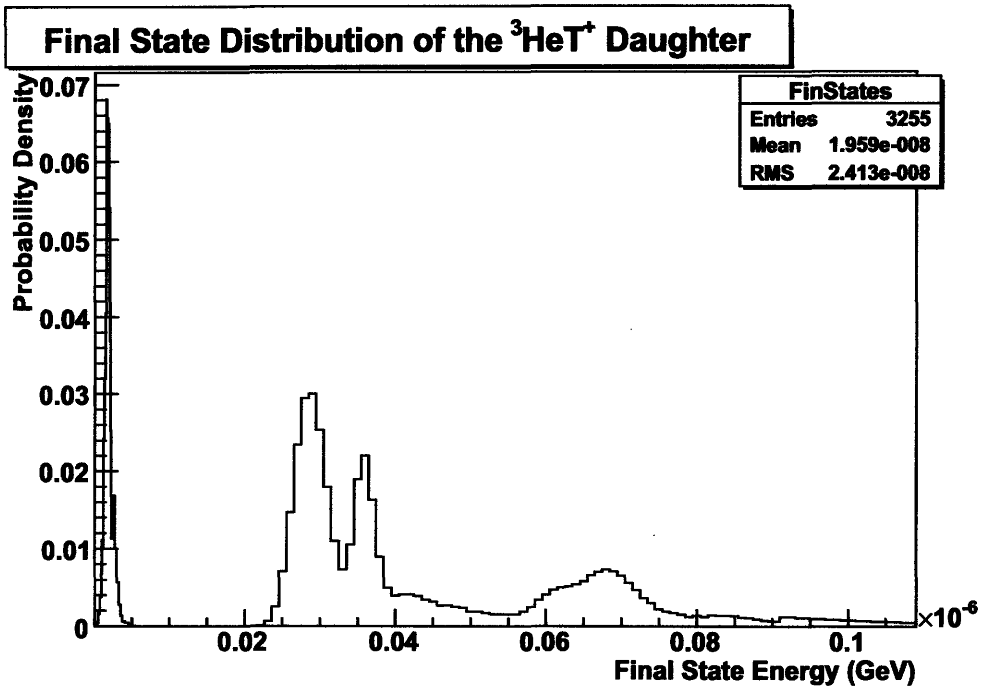

Figure 3-2: The distribution of final states of the $(^3HeT)^+$, constructed from Eq. 3.13 and the data given in 3.12.

Chapter 4

Thermal Motion and Doppler Shifts

The equation describing the beta spectrum of tritium decay, Eq. 2.1, is valid in the rest frame of the parent tritium. When the parent tritium is moving, it possesses more energy due to its kinetic energy, so the products of the decay must also have more energy in total. As discussed in Chapter 2, the tritium in the WGTS is moving for two reasons: random thermal motion, and the velocity profile due to pumping. Here we will consider the former. Because the source molecules are at a finite temperature, they possess a finite amount of thermal energy in the form of random motion. This random distribution of initial velocities translates into random shifts in the energy of the decay products, and so, tends to smear out the observed beta spectrum. This phenomenon is known as "Doppler broadening" of the spectrum. The name comes from the fact that, spectrometry is often performed to measure the spectrum of light, and so, the velocity of the light source causes a frequency shift (Doppler shift) in the frequency of the observed light. Even though the term "Doppler shift," strictly speaking, correspond to frequency shifts, the terminology is also used to describe spectrometry experiments in general; even those that measure energy spectra of particles, like KATRIN.

Therefore, because the initial velocity of the tritium gas molecule affects the energy of the emitted electron, a simulation of the electron energy spectrum requires a probability distribution for the initial velocities of the T_2 molecules. To this end, we can use the famous Maxwell velocity distribution. Because the T_2 gas in the WGTS consists of diatomic *molecules*, let us consider the significantly general treatment of the Maxwell velocity distribution performed in Ref. [16]. This treatment considers the effects of the internal energy states (see Chapter 3) of the T_2 molecule.

Even though the gas in the WGTS is of very high purity, this purity is not 100%. Therefore let us consider a general dilute gas, which consists of a mixture of different types of molecules. Let us then consider a polyatomic molecule of mass m (a T_2 molecule in our case) within this gas, with center of mass position and momentum $\vec{r}$ and $\vec{p}$ respectively. If this gas is sufficiently dilute such that it can be treated as ideal, then we may neglect intermolecular interactions. If we also neglect external forces, such as gravity, the energy of our particle is given by

$$E = \frac{\vec{p}^2}{2m} + E_{int} \tag{4.1}$$

where E_{int} represents the internal energy due to the rotational-vibrational state of the molecule. This internal state must be treated quantum mechanically, and is independent of position, due to the neglect of intermolecular interactions. However, due to the diluteness of the gas, the translational component of the molecule's state can be approximated to be classical, and the particle itself can be treated as a distinguishable particle.

The gas in the WGTS is maintained at a constant temperature, so the molecule is in contact with a heat reservoir, and therefore follows the canonical distribution. The canonical distribution states that a particle in contact with a heat reservoir of temperature T, has a probability to be in a state, α of

$$P_\alpha \propto e^{-\beta E_\alpha} \tag{4.2}$$

where $\beta = \frac{1}{k_b T}$, k_b is Boltzmann's constant, and E_α is the energy of state α. Applied to the T_2 molecule in the gas, this means that the probability of the molecule being in the volume $d^3\vec{r}$ centered about the position $\vec{r}$, having a momentum within the phase space volume $d^3\vec{p}$ centered about $\vec{p}$, and being in an internal quantum state denoted by the quantum number s is given by

$$P_s\left(\vec{r},\vec{p}\right) \propto e^{-\beta\frac{\vec{p}^2}{2m}} e^{-\beta E_{int}(s)} d^3\vec{r} d^3\vec{p} \tag{4.3}$$

In theory, the internal states of the T_2 molecule before it decays should affect the beta spectrum to some degree. However, the value of the rest mass of T_2 that is currently used in KATRIN analysis is simply twice the rest mass of atomic tritium, T.[17, 18, 10] This is only approximately correct as it neglects the binding energy of T_2, which is estimated to be negligible compared to uncertainties in other quantities used in the calculations.[18] Therefore, the effects of the initial internal states of T_2 would be beyond the precision of the rest energy of T_2, and so the inclusion of these effects at this stage would be artificial and require a more detailed knowledge of T_2. Therefore, in the simulations in this thesis, the initial internal states of T_2 are neglected.

Therefore, to get the probability for a certain position and momentum range only, we sum over all states s in Eq. 4.3. The result is simply an overall constant which is irrelevant, for the final probability density will be normalized. We may also integrate over $\vec{r}$ since we are interested in obtaining the velocity distribution, which is a function of $\vec{v} = \frac{\vec{p}}{m}$ only. The result is simply the product of three identical Gaussian distributions, one for each component of the velocity. Normalization results in the Maxwell velocity distribution: the probability for a molecule to have a velocity in a range $d^3\vec{v}$ about a value of $\vec{v}$ is[16]

$$f_{mv}(\vec{v})d^3\vec{v} = \left(\frac{m}{2\pi k_b T}\right)^{3/2} e^{-\frac{m\vec{v}^2}{2k_b T}} d^3\vec{v} \tag{4.4}$$

If we are only interested in the speed of the particle, then we can change from Cartesian to spherical coordinates ($d^3\vec{v} = v^2 \sin\theta dv d\theta d\phi$) and integrate over all directions (over θ and ϕ) to obtain the Maxwell speed distribution[16]

$$f_{ms}(v)dv = \left(\frac{m}{2\pi k_b T}\right)^{3/2} \cdot 4\pi v^2 e^{-\frac{mv^2}{2k_b T}} dv \tag{4.5}$$

Which gives the probability for the particle to have a speed between v and $v + dv$.

These are the velocity distributions used in this thesis to determine the random thermal velocities. This will also be used in the next chapter in the analysis of the fluid velocity profile. Note that we are able to use these standard forms of the Maxwell distributions because we neglected the initial states and the effect of gravity. To correct for gravity, one could include a term of the form $e^{-\beta mgz}$, where g is the acceleration due to gravity. However, this is unnecessary, because the change in gravitational potential over the diameter of 0.09m is negligible and inclusion of this factor would just add fruitless computation time to the simulation. Also, if one were to include the initial states of T_2, one would have to return to Eq. 4.3, or include an independently constructed distribution of initial states.

Chapter 5

Velocity Profile Due to Pumping

As discussed above, in addition to random thermal motion, the tritium molecules' motion is also determined by the pumping systems at the ends of the WGTS. This pumping establishes a pressure gradient which, in turn, exerts a force on the tritium, establishing a velocity profile. Since this pressure gradient is the driving force behind the velocity profile, we must first estimate the pressure profile within the WGTS in order to estimate the velocity profile. We will model the tritium gas as an ideal gas (as done in the previous chapter), which then follows the equation

$$P = nk_bT \tag{5.1}$$

Where P is pressure, n is the number density of the gas, and T is the temperature. Furthermore, since the temperature is constant within the tube, the pressure profile is simply the density profile multiplied by a *constant* factor of k_bT, where T = 27K. We will now follow the calculations performed in [10], with slight modification, in order to estimate the pressure profile within the WGTS.

5.1 The Density/Pressure Profile

In these calculations a number of assumptions are made, some of which are only approximations of the WGTS setup. First, the length of the tube, 10m, is assumed to be much larger than the radius of the tube, 0.045m so that end effects can be neglected, making the flow essentially one-dimensional. This assumption means that the density does not vary within any cross section of the gas and that the *local* pressure gradient, ν, is small, even though the entire pressure drop along the tube is quite large.[10] Quantitatively, this is

$$\nu = \frac{R}{P}\frac{dP}{dz} \ll 1 \tag{5.2}$$

where P is the pressure and R is the radius of the WGTS tube (0.045m). This assumption is only approximately true, however, since the ratio of length to ratio is only approximately 220. Later, we will partially lift this assumption by using the density profile generated here to construct a two-dimensional velocity profile. This is similar in spirit to perturbation theory; we approximate the solution to a difficult problem by taking the solution to a simpler, related problem and plugging it in to higher order calculations.

Another assumption that is made is that, since the *total* pressure drop, from the injection point to the ends of the WGTS, will be large (in other words $P_{ex} \ll P_{in}$), we will set $P_{ex} = 0$ in the following calculations. Here, we use the notation that P_{in} is the pressure at the injection site, and P_{ex} is the pressure at the exit points (the ends of the WGTS tube). This, of course, is another approximation; P_{ex} is not actually zero. Another assumption made is that the interaction between the tritium gas and the metal surface of the WGTS tube is diffuse; i.e. the accommodation coefficient, α, is equal to 1. This is done because the accommodation coefficient for such an interface is not known. [10] One final assumption is that the temperature is constant throughout the WGTS, which is a relatively reasonable assumption, since the temperature will be maintained within stability to 0.1%. [10, 6] Since the total pressure drop is large, we can analyze this system within the model of rarefied flow developed in Ref. [19]. (Rarefaction is the decrease of a fluid's density; i.e. the opposite of compression).

The local rarefaction parameter, $\delta(z)$ is defined as

$$\delta(z) = \frac{rP(z)}{\mu v_m} \tag{5.3}$$

Where μ is the viscosity, and v_m is the most probable molecular velocity, defined as

$$v_m = \left(\frac{2R_gT}{m}\right)^{1/2} \tag{5.4}$$

R_g is the gas constant ($R_g = 8.314$ J/(K mol)), m is the mass of molecular tritium (m $\simeq$ 6 a.m.u. $=$ 6g/mol), and T is the temperature (27K). The general strategy of Ref. [10] is to introduce the reduced flow rate, G, and the local reduced flow rate, $G_P(\delta)$ (defined in Eqs. 5.5, 5.6) , derive a relation between them, and then integrate along the WGTS tube (since G does not vary in our model).

$$G = \frac{v_m(L/2)}{\pi r^3 P_{in}}\dot{M} \tag{5.5}$$

$$G_P(\delta) = \frac{-v_m}{\pi r^2 \nu}\frac{1}{P(z)}\dot{M} \tag{5.6}$$

Here, L is the length of the WGTS tube (10m), and $\dot{M}$ is the mass flow rate through a cross section of the tube. Combining together Eqs. 5.2, 5.5, 5.6 yields the relation

$$G_P\frac{(L/2)}{\delta_{in}}\frac{d\delta}{dz} = -G \tag{5.7}$$

Here, δ_{in} is the rarefaction parameter at the injection site (related to P_{in} through Eq. 5.3). Eq. 5.7 can then be integrated (recall that G is constant in z) from the injection point to an arbitrary point z to obtain

$$\frac{1}{\delta_{in}}\int_{\delta_{in}}^{\delta} G_P(\delta)\, d\delta = -\frac{z}{(L/2)}G \tag{5.8}$$

We then quote a result from Ref. [19]

$$\int_{\delta_1}^{\delta_2} G_P(\delta)\, d\delta = (\delta_2 - \delta_1)G_P\left(\frac{\delta_1+\delta_2}{2}\right) \tag{5.9}$$

Now, using Eqs. 5.8 and 5.9, we have

$$z = (L/2)\left(1 - \frac{\delta}{\delta_{in}}\right)\frac{G_P\left(\frac{\delta_{in}+\delta}{2}\right)}{G_P\left(\frac{\delta_{in}}{2}\right)} \tag{5.10}$$

This is an equation for $z(\delta)$. Using knowledge of the functional form of $G_P(\delta)$, this equation can be inverted to obtain $\delta(z)$. Then Eq. 5.3 can be used to obtain the pressure profile, P(z). All that remains now is to determine a functional form of $G_P(\delta)$. Ref. [20] surveys the data and analysis performed in various papers to calculate $G_P(\delta)$. The following form of G_P is obtained from the Navier-Stokes equation and is presented by Ref. [20] for use in the hydrodynamic limit

$$G_P(\delta) = \frac{\delta}{4} + \sigma_P \tag{5.11}$$

Here, σ_P is the slip coefficient, which is equal to 1.018 (when the accommodation coefficient, α, is equal to 1, as we are assuming it to be).[10] Thus, by using the functional form of $G_P(\delta)$ given in Eq. 5.11, Eq. 5.10 can be inverted and combined with Eq. 5.3 to finally yield a functional form of the pressure profile P(z).

$$P(z) = A + \sqrt{B - C\left(\frac{z}{L} - \frac{1}{2}\right)} \tag{5.12}$$

Where A, B, and C are constants. Note, however, that, since Eq. 5.11 is only valid in the hydrodynamic limit, the functional form, Eq. 5.12, is also valid only in the hydrodynamic limit.

Ref. [10] performs numerical analysis and determines that, in the WGTS, the tritium gas at the injection point falls within the hydrodynamic regime, but along the tube, there is a transition to the free molecular regime. Values of G_P for the free molecular and transitional regimes are also given. All of this is combined together to create a plot (Fig. 5.1) of the scaled density profile $n(z)/n_{in}$ that the author feels is representative of the density profile in the WGTS.[10, 21]

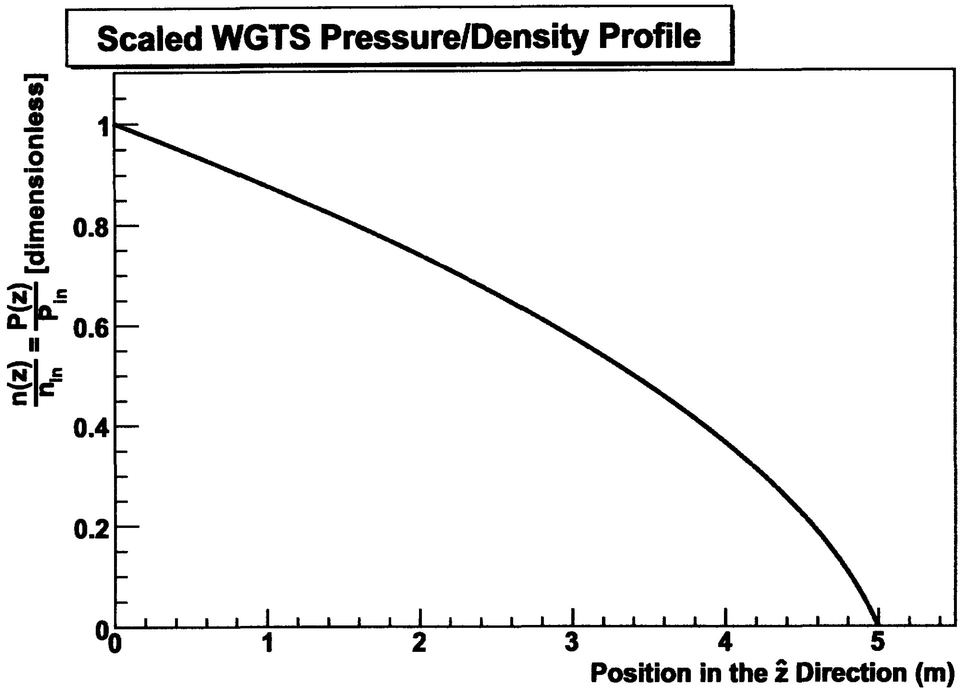

Figure 5-1: Scaled Density/Pressure profile. This plot was constructed from the data from Ref. [10, 21]

5.2 The Viscosity of Tritium

Unfortunately, the value of the viscosity of tritium (μ in the above equations) is unknown. Currently, there are no experimental measurements. Therefore, we must estimate μ based on known viscosities of other gases, such as deuterium. To do this, we must first determine the way in which the viscosity of a fluid depends on the fundamental parameters of its constituent molecules. We will do this here using the standard momentum diffusion model of viscosity. When viscous fluids flow along a wall, the interactions between the molecules in the wall and those in the fluid slow down the fluid flow at the boundary. Empirically, the shear stress, F, that slows the fluid is shown to be of the form [23]

$$F = -\mu \frac{\partial u_z}{\partial r} \tag{5.13}$$

Consider, for example, the tritium flow in the WGTS, Fig. 2-2. The fact that the fluid moves slower near the walls means that there exists a momentum gradient along the $\hat{r}$ direction (perpendicular to the flow). Viscosity can be viewed as the diffusion of the $\hat{z}$ component of momentum due to this gradient, because such a diffusion would also cause the change in velocity. Due to thermal energy, the molecules of a fluid move about randomly with an average speed of $\bar{v}$ with respect to the fluid velocity. We estimate $\bar{v}$ by equating the average kinetic energy, $\frac{1}{2}m\bar{v}^2$, of such motion to the thermal energy, k_bT to obtain [24]

$$\bar{v} = \sqrt{\frac{2k_bT}{m}} \tag{5.14}$$

The mean free path, λ is the average distance a molecule travels through a medium (here, the fluid) between two scattering events. The scattering cross-section, σ, of the molecules in the fluid is defined by the relation that there should exist one collision center within a volume $\lambda\sigma$. In terms of the density, n of the molecules, this relation becomes: [23]

$$\lambda = \frac{1}{\sigma n} \tag{5.15}$$

We then argue that the $\hat{z}$ momentum carried across the distance of the mean free path in the $\hat{r}$ direction is the difference in momenta, given by $m\frac{\partial u_z}{\partial r}\lambda$. Since the molecules move randomly via thermal motion with a speed of $\bar{v}$, the flux of this momentum should be proportional to $\bar{v}$. And, so, taking the momentum difference and multiplying it by the characteristic speed, we obtain [23]

$$F \propto \bar{v}m\frac{\partial u_z}{\partial r}\lambda \propto \frac{\sqrt{2mk_bT}}{\sigma} \tag{5.16}$$

Comparing this to Eq. 5.13 yields

$$\mu \propto \frac{\sqrt{mk_bT}}{\sigma} \tag{5.17}$$

Thus, if we assume that deuterium and tritium, which differ by one neutron, have the same cross-section, σ, then the ratio of their viscosity coefficients, μ, is simply given by the square root of the ratio of their masses (by Eq. 5.17). Since the viscosity coefficient, μ_D, of deuterium is known, we can estimate the viscosity of tritium to be [10]

$$\mu_T = \sqrt{\frac{m_T}{m_D}}\mu_D = 2.425 \cdot 10^{-6} Pa \cdot s \tag{5.18}$$

5.3 The Velocity Profile

Calculation of an exact velocity profile for the tritium flow within the WGTS is a difficult and computationally-intensive task that is beyond the scope of this thesis. [10] There are many technical challenges involved. For instance, recall that Ref. [10] concludes that the tritium flow transitions from the hydrodynamic regime to the free molecular regime within the WGTS. Therefore, even an exact solution to the Navier-Stokes Equation (see below) would not even be valid throughout the entire length of the WGTS. To obtain a near-exact profile, the hydrodynamic, transitional, and free molecular regions, along with their interfaces, would each have to be analyzed with different models. Therefore, in this thesis, an approximated velocity profile, based on the hydrodynamic limit, will be obtained and applied to the entire WGTS. In this way, we can obtain an estimate of the velocity profile that will be sufficient for our purposes.

5.3.1 The Navier-Stokes Equation

In the hydrodynamic limit, viscous fluid flow is governed by the Navier-Stokes Equation:[23]

$$\left(\frac{\partial}{\partial t} + \vec{u} \cdot \vec{\nabla}\right)\vec{u} + \frac{1}{\rho}\vec{\nabla}\left(P - \frac{\mu}{3}\vec{\nabla} \cdot \vec{u}\right) - \frac{\mu}{\rho}\nabla^2\vec{u} = \frac{\vec{F}}{m} \tag{5.19}$$

Where P is pressure, F is the external force, ρ is mass density, and $\vec{u}$ is the velocity of the fluid. This equation is highly nonlinear and notoriously difficult to solve in general. However, the WGTS geometry is an axially symmetric tube with a constant circular cross-section. Incompressible viscous flow through such a geometry is classified as

Poiseuille flow.[26] In this geometric context, Eq. 5.19 greatly simplifies to:[26]

$$\frac{dP}{dz} = \mu \frac{d^2u}{dr^2} \tag{5.20}$$

This equation can be easily integrated if the pressure gradient, $\frac{dP}{dz}$, is independent of r. All that is left to determine is the boundary conditions for Eq. 5.20. To accomplish this task, we will follow the derivation in Ref. [26], which presents a new slip model for rarefied gas flow.

5.3.2 The Boltzmann Transport Equation

A very rigorous treatment of transport processes by examining molecule-molecule collisions leads to the derivation of the Boltzmann Transport Equation:[25]

$$\left(\frac{\partial}{\partial t} + \frac{\vec{p_1}}{m} \cdot \vec{\nabla}_r + \vec{F} \cdot \vec{\nabla_{p1}}\right) f_1 = \int d^3p_2 d^3p'_1 d^3p'_2 \delta^4(P_f - P_i)|T_{fi}|^2 (f'_2 f'_1 - f_2 f_1) \tag{5.21}$$

Here, $f_1 \equiv f(\vec{r}, \vec{p_1}, t)$, $f_2 \equiv f(\vec{r}, \vec{p_2}, t)$, $f'_1 \equiv f(\vec{r}, \vec{p'_1}, t)$, and $f'_2 \equiv f(\vec{r}, \vec{p'_2}, t)$. Where the subscripts denote two colliding particles, and the primes denote quantities after the collision. T denotes the quantum-mechanical transition matrix, and f_i is the distribution function of particle i.

This equation governs transport phenomena subject to the following assumptions. Any external forces should act on all of the particles in a similar fashion, so any effect of these forces on the collision cross-section may be ignored. The gas is dilute enough so that only two-particle collisions need to be considered. The variation of f over a the timescale of molecular collisions or length scale of intermolecular forces is negligible. And, finally, there is the assumption of "molecular chaos," which states that any correlation between the initial velocities of two colliding molecules is negligible. [16, 25]

5.3.3 Boundary Conditions

Ref. [26] begins with Eq. 5.21 and derives boundary conditions, in general, for Poiseuille flow. Then, Eq. 5.20 is integrated to yield an analytic expression for the velocity profile. Because this derivation is based on general Poiseuille flow and is not specific to the WGTS in KATRIN, I will only sketch out the derivation, focusing on steps where assumptions are made. I will also discuss the applicability of these assumptions to the WGTS.

Assuming that the flow velocity is significantly smaller than the constituent molecules' thermal velocities, Eq. 5.21 can be approximated by

$$\frac{\partial f}{\partial t} + \frac{d\vec{r}}{dt} \cdot \vec{\nabla}_r f + \frac{d\vec{v}}{dt} \cdot \vec{\nabla}_v f = -\frac{f - f_d}{\tau} \tag{5.22}$$

where $f_d = f_d(\vec{v}) = n \cdot f_{mv}(\vec{w})$ where f_{mv} is given by Eq 4.4. This is known as the Krook equation. Here, $\vec{v}$ is the total velocity of a molecule, $\vec{u}$ is the flow velocity, and $\vec{w}$ is the thermal velocity of a molecule, and the three are related by $\vec{w} = \vec{v} - \vec{u}$. $/tau$ is the relaxation time, which is the average time that a molecule spends between collisions. In general, τ may be a function of the speed of the molecule.[16]

It is worth noting that the assumption that the flow velocity is small compared to the thermal velocity breaks down for the regions of faster fluid flow near the ends of the WGTS. The velocities that this slip model predicts for these regions are larger than the thermal velocities. However, these regions of deviation near the exit points fall within the free molecular regime.[10] So, for the purposes of this derivation, we can ignore discrepancies in these regions, since we are aware that, within these regions, the velocity profile is only an estimate and *any* hydrodynamic model will break down here. Within the hydrodynamic region of the WGTS, the fluid velocity predicted by this model is more than one order of magnitude smaller than the thermal velocities.

Ref. [26] then quotes a solution to this equation which further simplifies under the assumptions that $\frac{du}{dz}$ is negligibly small, P=P(z), and temperature is constant. The result is

$$f = f_d - n \cdot f_{mv}(\vec{v})\tau(v_z - u)v_r \frac{m}{kT}\frac{du}{dr} \tag{5.23}$$

Where $f_{mv}(\vec{v})$ is the Maxwell Velocity Distribution given in Eq. 4.4. For the WGTS, the assumptions that P=P(z) and T is constant are consistent with assumptions made above by Ref. [10] in deriving the pressure/density profile in Fig. 5.1. The assumption that $\frac{du}{dz}$ is negligible is similar to the assumption made in Eq. 5.2 by Ref. [10]. The arguments run parallel. The way in which the pressure changes along the tube (in the $\pm\hat{z}$ direction) is what influences the velocity profile to vary along the tube. Since we have already assumed that the pressure changes slowly along the length of the *entire* tube, it seems reasonable to say that the velocity should also change sufficiently slowly along the length of the tube. Therefore, $\frac{du}{dz}$ should also be negligible within our model of the WGTS. In this way, as in the pressure profile, we can neglect $\frac{du}{dz}$ and arrive at a velocity profile that does have z-dependence, but only on a relatively long length scale.

Next, Eq. 5.23 can be used to calculate an expression for the shear stress (Eq. 5.13). This will yield a useful expression for the viscosity of this system, μ, in terms of the macroscopic quantities n and T.

$$F = -\int m v_y (v_z - u) f, d^3v = n\tau k_b T \frac{du}{dr} \tag{5.24}$$

Comparing this to Eq. 5.13 yields the following expression for viscosity

$$\mu = n\tau k_b T \tag{5.25}$$

Ref. [26] then proceeds by setting up an imaginary boundary region and calculating the corresponding shear stresses for that region using expressions similar to Eq. 5.24. In calculating these expressions a derivative of Eq. 5.23 is taken to obtain

$$\frac{df}{dz} \simeq \frac{df_d}{dz} \simeq f_d \left[\frac{1}{nk_bT}\frac{dP}{dz}\right] \tag{5.26}$$

In taking this derivative, the high order term $\frac{du}{dr}\frac{dP}{dz}$ was neglected. This is perfectly consistent with our assumptions for the WGTS (Eq. 5.2). It was also once again assumed that $\frac{du}{dz}$ is negligible, which as argued above, is also reasonably applicable the WGTS. The analysis of the expressions for the shear stresses on the imaginary boundary region ultimately results in the boundary condition:

$$u\left(r=\pm\frac{D}{2}\right)=\pm\frac{2-\alpha}{\alpha}\tau\left(\frac{\pi k_b T}{2m}\right)^{1/2}\frac{du}{dr}-\frac{\pi\tau D}{\alpha mn\left[2\tau\left(\frac{\pi k_b T}{2m}\right)^{1/2}+sqrt3D\right]}\frac{dP}{dz} \tag{5.27}$$

Here, α is the accommodation coefficient of the wall of the WGTS. Using these boundary conditions with Eq. 5.20, and eliminating τ with Eq. 5.25, the final result (simplified for the WGTS geometry and with $\alpha = 1$) is:

$$\frac{-1}{2\mu}\frac{dP}{dz}\left[\frac{D^2}{4}-r^2+AD+2\mu B\right] \tag{5.28}$$

With

$$A=\left(\frac{\pi k_b T}{2m}\right)^{1/2}\frac{\mu}{P} \tag{5.29}$$

$$B=\frac{\pi D\mu k_b T}{m\left[2A+\sqrt{3}D\right]}\frac{1}{P^2} \tag{5.30}$$

Chapter 6

Results & Analysis

6.1 The Density and Velocity Profiles

The velocity profile in Eq. 5.28 requires a z derivative of Pressure. To perform this derivative, a table of values (Ref. [21]) for Fig. 5.1 was used as input to a spline interpolation tool, which interpolates the first derivative of the data at a given point. Using this tool, the derivative shown in Fig. 6.1 was obtained.

A sample result of Eq. 5.28 is shown in Fig. 6.1. This is the velocity as a function of r for z = L/4, where L is the length of the WGTS.

The density profile (Fig. 5.1) was used to determine the probability of a decay as a function of position. In these simulations, a linear weighting in r was also used due to the fact that our coordinate system is a 2D representation of a geometry with a circular cross section. A scatter plot of the result of the combination of these two profiles is shown in Fig. 6.1. Note the high density near the center injection point.

6.2 The Beta Spectra

My analysis of the Doppler shifts consists of a full simulation of the beta decay of T_2, including both the phase space factor and the dot-product factor in Eq. 3.6. First a random position of the parent T_2 is chosen based on the considerations discussed above. This position is then fed into Eq. 5.28 to determine the flow velocity. A

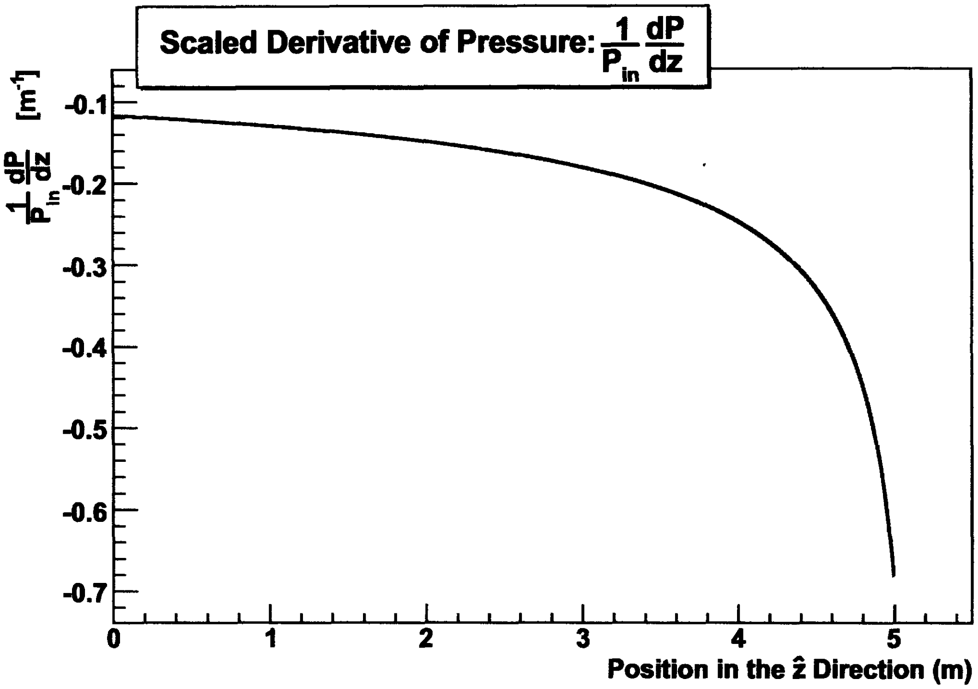

Figure 6-1: Scaled z derivative of Pressure. This plot was constructed by using a spline interpolator tool with the data corresponding to Fig. 5.1

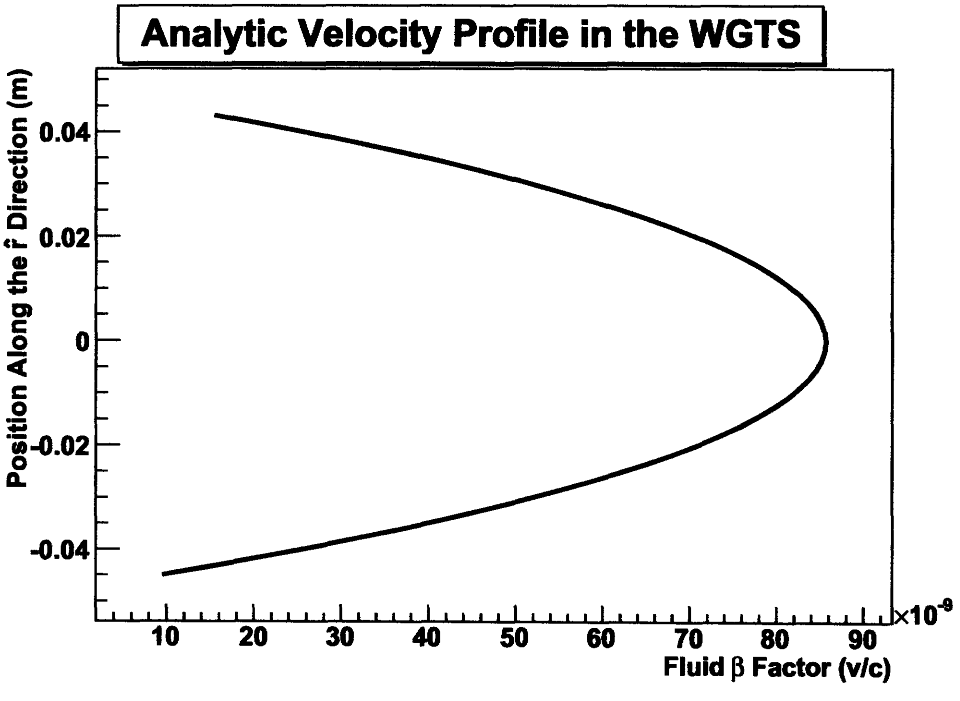

Figure 6-2: The flow velocity for tritium gas in the WGTS given by Eq. 5.28, evaluated at z = L/4, where L is the length of the WGTS.

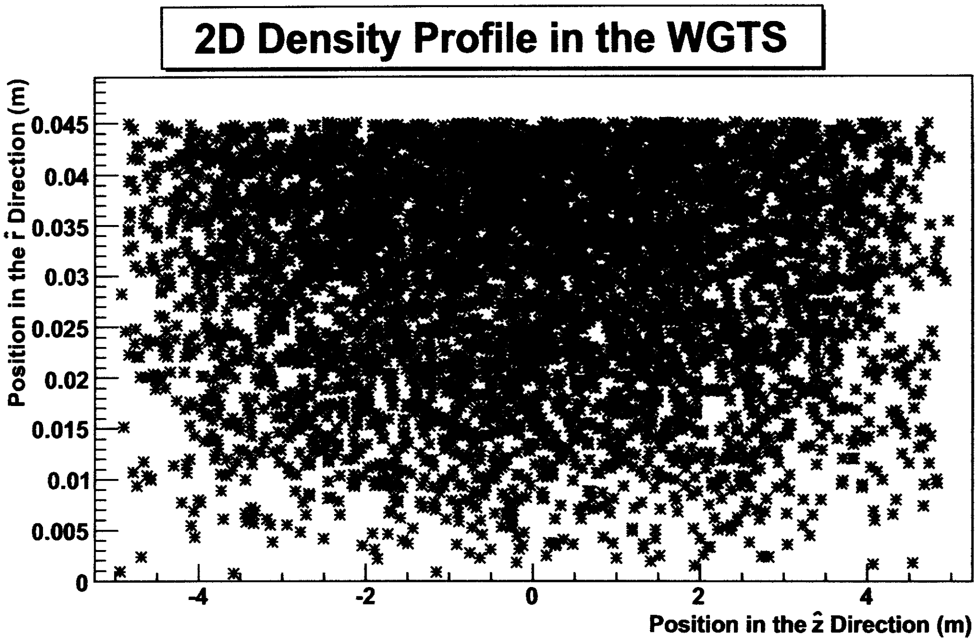

Figure 6-3: A scatter plot of the distribution of particles within our 2D slice of the WGTS.

random thermal velocity is chosen from Eq. 4.4 to be added to the flow velocity to give the total initial velocity of the T_2 before it decays. A random rest energy of the $(^3HeT)^+$ is chosen from the final state distribution, Fig. 3.5. The decay T_2 is then simulated in the rest frame of the T_2. Then all three decay products are boosted back into the laboratory frame using the initial velocity of the T_2. This boosting is the full Lorentz velocity transformation. Then this final electron energy, after the boost transformation, is recorded in a histogram. To study the effects of these two different velocity considerations (thermal and flow), a number of simulations were performed, for three values of the neutrino mass.

6.2.1 Inclusion of the Final State Distribution

When the final state distribution was included in the simulation, the endpoint was blurred due to the effects discussed in Chapter 3. Preliminary runs of these simulations showed that this blurring due to final states had the effect of washing out the velocity effects, Figs. 6.2.1, 6.2.1. These results showed that a study of the velocity-

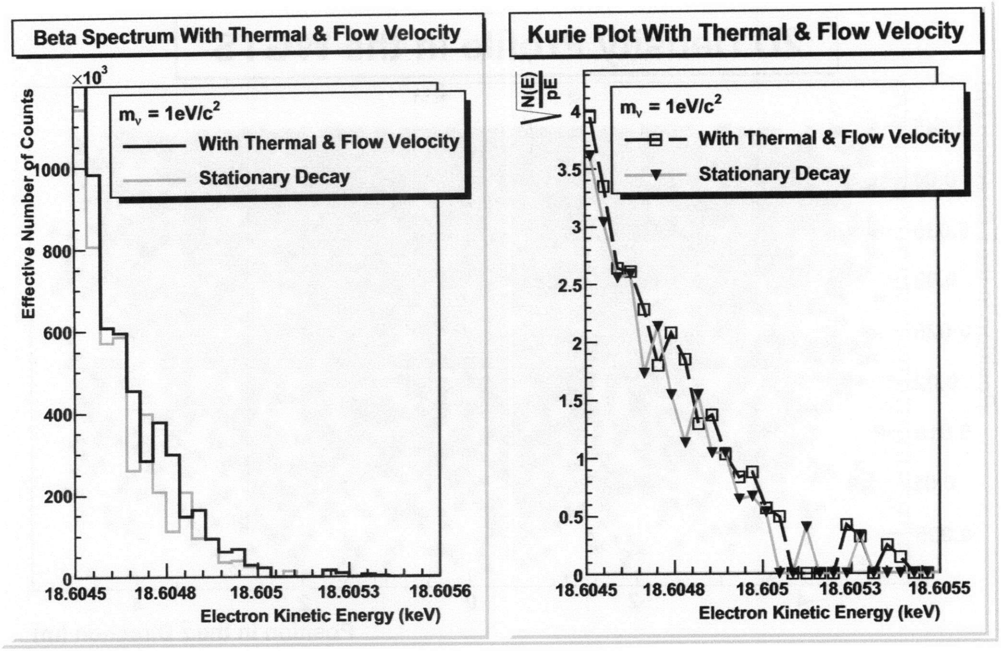

Figure 6-4: For a neutrino mass of 1eV$/c^2$, the distortion of the beta spectrum, and corresponding Kurie plot, due to the influenced of thermal motion, flow velocity, and the final state distribution. These beta specra were constructed with $5 \cdot 10^9$ decay events.

related effects which also incorporates the final state distribution requires statistics that are too large to be produced given the time and computational resources available for this thesis. Therefore, to present more vivid and numerous examples of the velocity-related effects, we will examine, in the next section, spectra that do *not* include the final state distribution.

/subsectionNeglecting the Final State Distribution To obtain a clearer picture of the sources of the Doppler shifts, we will examine, for each neutrino mass, beta decays from stationary T_2 molecules (the control dataset), T_2 influenced by thermal velocities (Eq. 4.4) alone, T_2 influenced by the flow velocity alone (Eq. 5.28), and T_2 molecules influenced by both of these velocities. The results of this analysis is shown in Figs. 6.2.1-6.2.1.

The spectra are given here in "effective" number of counts. This is due to the fact that, in the creation of these histograms, instead of throwing out events, each event was given a weighting and a weighted histogram was created. The effective counts

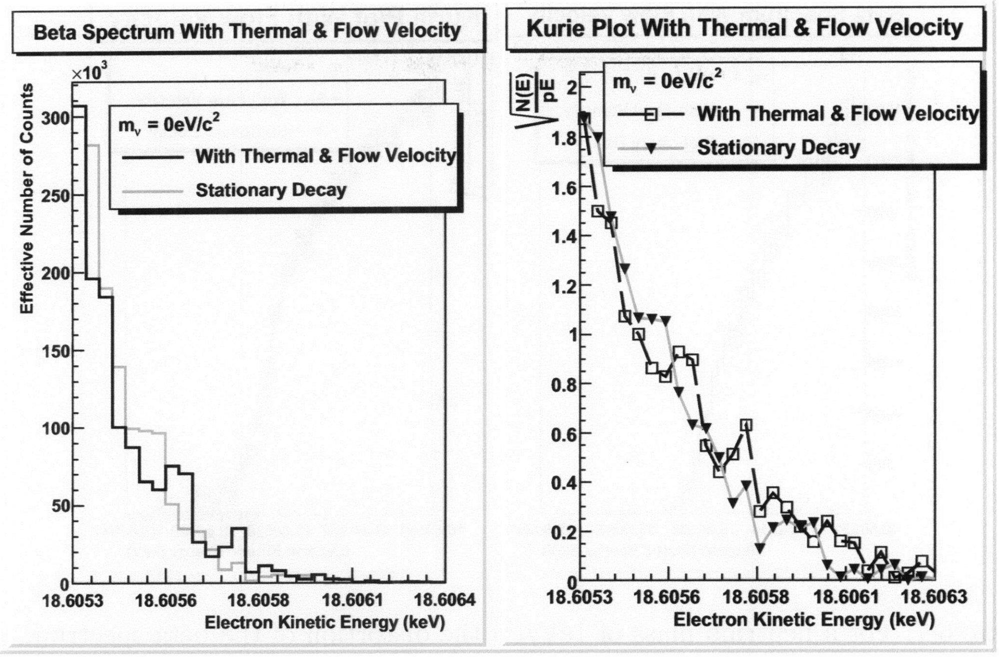

Figure 6-5: For a neutrino mass of $0\text{eV}/c^2$, the distortion of the beta spectrum, and corresponding Kurie plot, due to the influenced of thermal motion, flow velocity, and the final state distribution. These beta specra were constructed with $5 \cdot 10^9$ decay events.

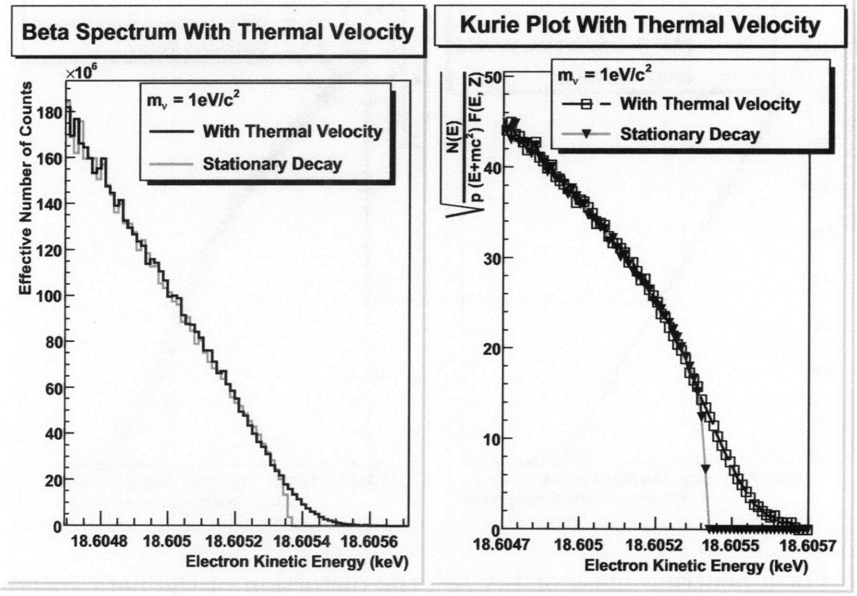

Figure 6-6: For a neutrino mass of $1\text{eV}/c^2$, the distortion of the beta spectrum, and corresponding Kurie plot, due to the influenced of thermal motion only. These beta specra were constructed via $7 \cdot 10^9$ decay events.

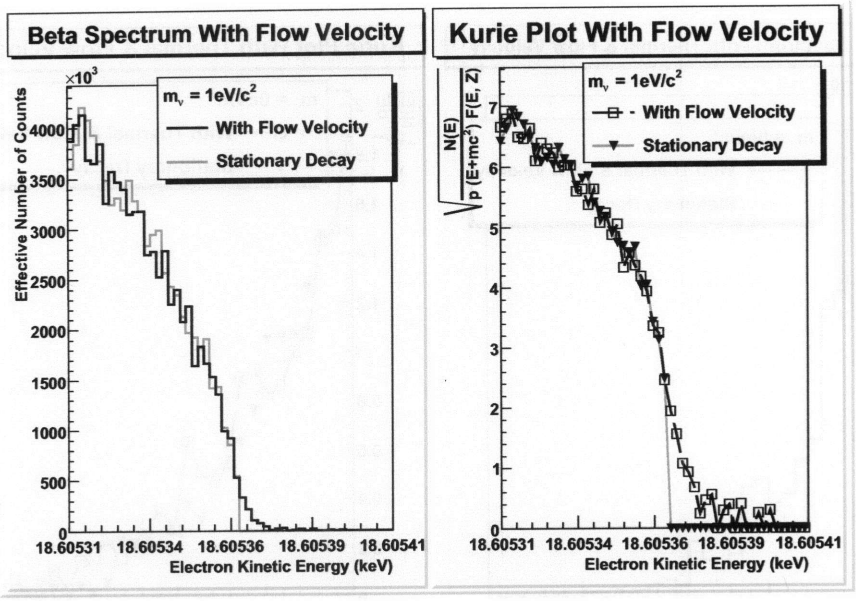

Figure 6-7: For a neutrino mass of $1\text{eV}/c^2$, the distortion of the beta spectrum, and corresponding Kurie plot, due to the influenced of the flow velocity only. Note that the scale of the energy axis of this figure is an order of magnitude less than the other figures considered in this section. These beta specra were constructed via $7 \cdot 10^9$ decay events.

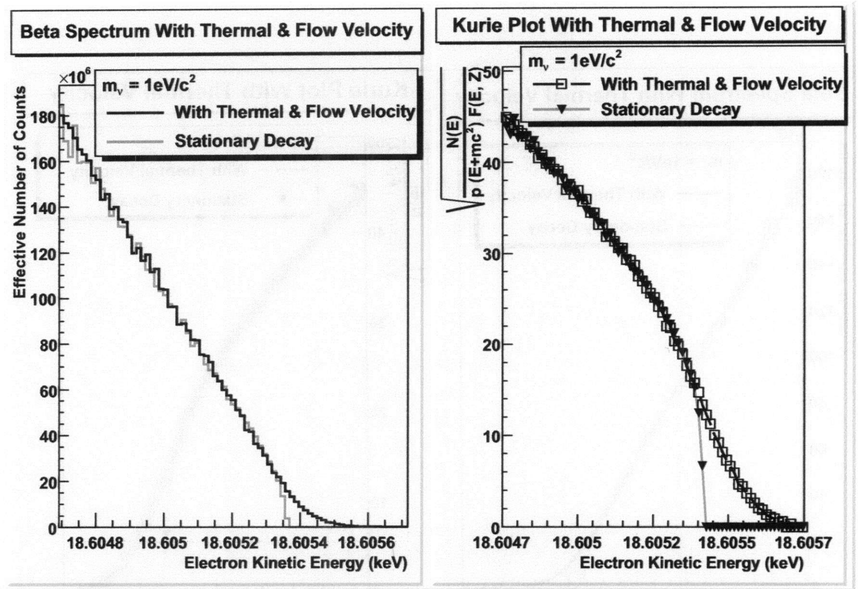

Figure 6-8: For a neutrino mass of $1\text{eV}/c^2$, the distortion of the beta spectrum, and corresponding Kurie plot, due to the influenced of both thermal motion and the flow velocity. This is the result of direct simulations of the two simultaneous effects, and was *not* obtained by simply adding Fig. 6.2.1 and Fig. 6.2.1. These beta specra were constructed via $7 \cdot 10^9$ decay events.

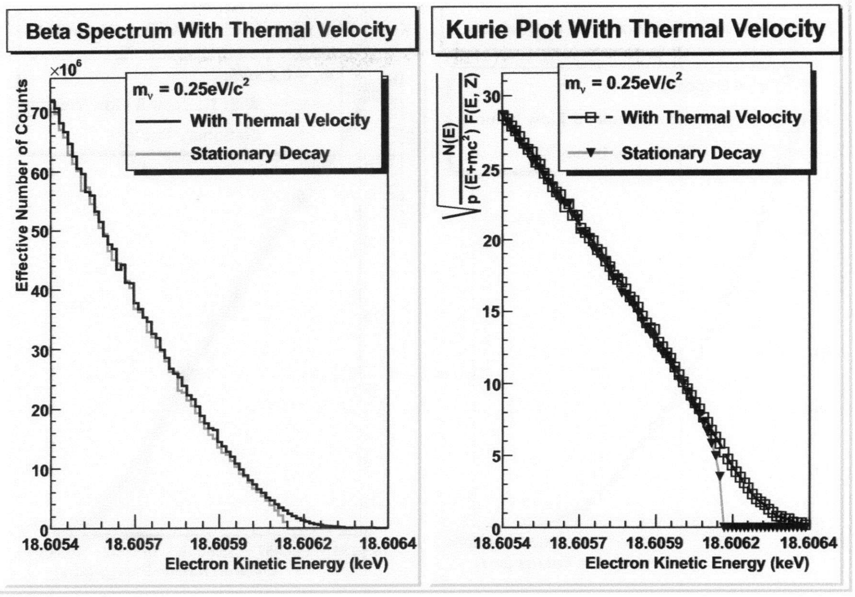

Figure 6-9: For a neutrino mass of $0.25\text{eV}/c^2$, the distortion of the beta spectrum, and corresponding Kurie plot, due to the influenced of thermal motion only. These beta specra were constructed via $7 \cdot 10^9$ decay events.

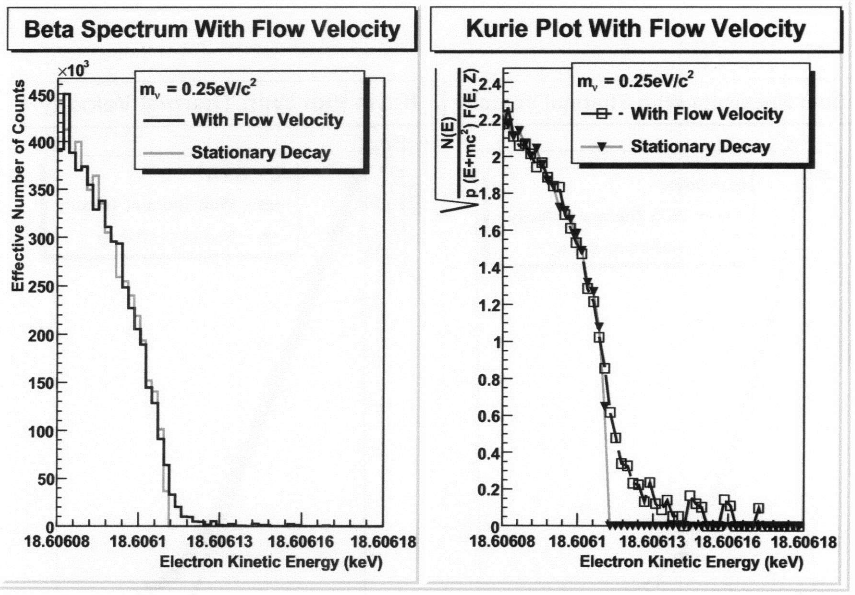

Figure 6-10: For a neutrino mass of $0.25\text{eV}/c^2$, the distortion of the beta spectrum, and corresponding Kurie plot, due to the influenced of the flow velocity only. Note that the scale of the energy axis of this figure is an order of magnitude less than the other figures considered in this section. These beta specra were constructed via $7 \cdot 10^9$ decay events.

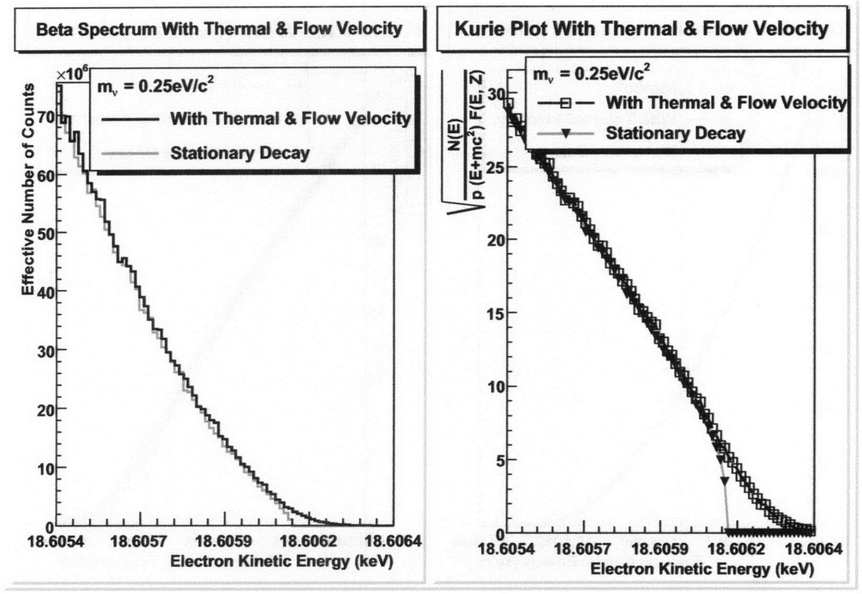

Figure 6-11: For a neutrino mass of 0.25eV$/c^2$, the distortion of the beta spectrum, and corresponding Kurie plot, due to the influenced of both thermal motion and the flow velocity. Again, this is the result of direct simulations of the two simultaneous effects, and was *not* obtained by simply adding Fig. 6.2.1 and Fig. 6.2.1. These beta specra were constructed via $7 \cdot 10^9$ decay events.

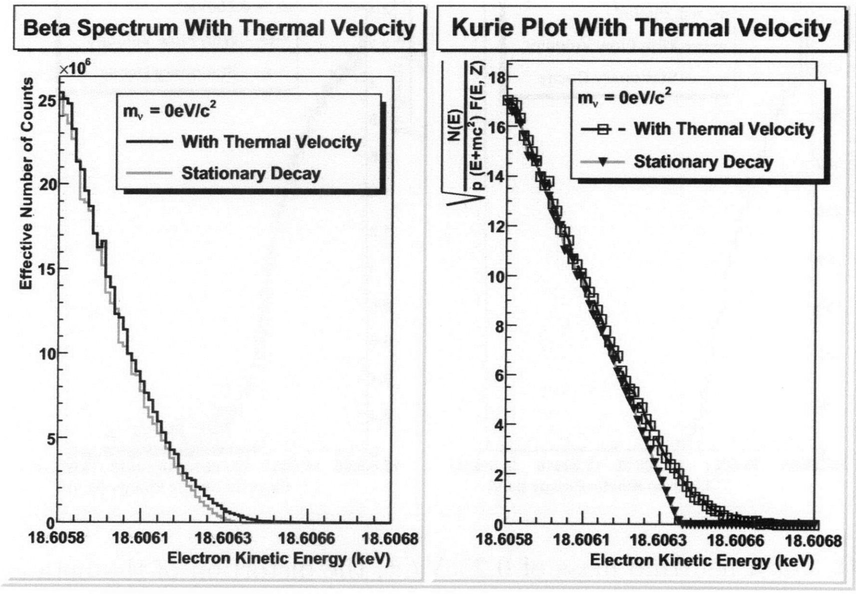

Figure 6-12: For a neutrino mass of 0eV$/c^2$, the distortion of the beta spectrum, and corresponding Kurie plot, due to the influenced of thermal motion only. These beta specra were constructed via $7 \cdot 10^9$ decay events.

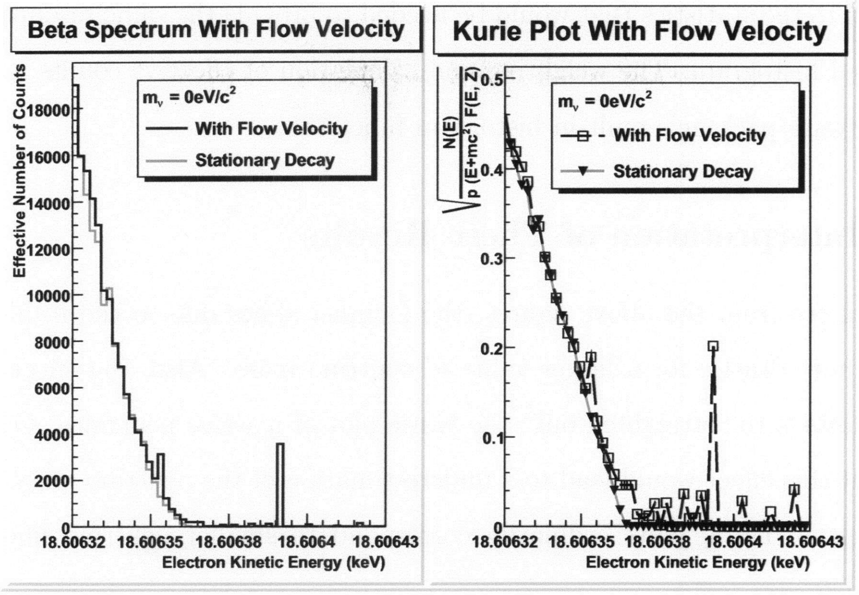

Figure 6-13: For a neutrino mass of $0\text{eV}/c^2$, the distortion of the beta spectrum, and corresponding Kurie plot, due to the influenced of the flow velocity only. Note that the scale of the energy axis of this figure is an order of magnitude less than the other figures considered in this section. These beta specra were constructed via $7 \cdot 10^9$ decay events.

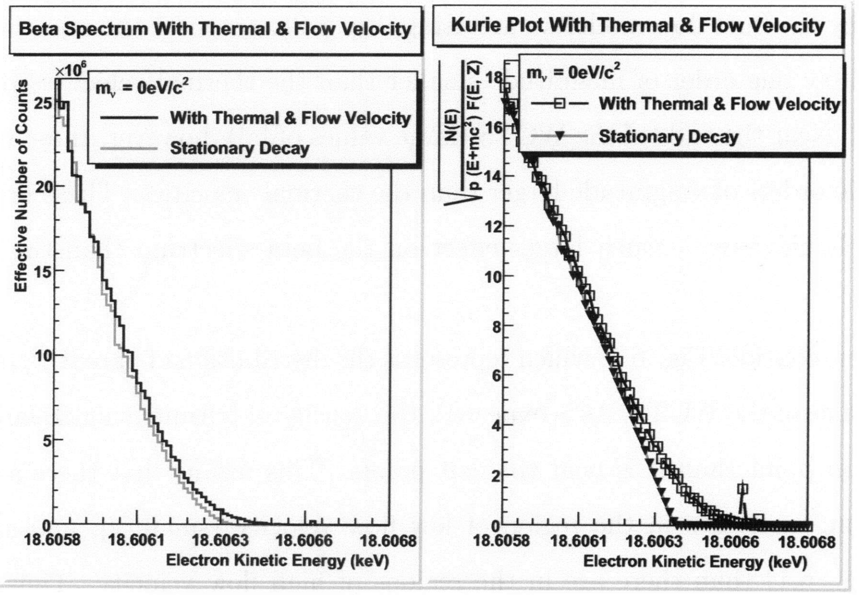

Figure 6-14: For a neutrino mass of $0\text{eV}/c^2$, the distortion of the beta spectrum, and corresponding Kurie plot, due to the influenced of both thermal motion and the flow velocity. Again, this is the result of direct simulations of the two simultaneous effects, and was *not* obtained by simply adding Fig. 6.2.1 and Fig. 6.2.1. These beta specra were constructed via $7 \cdot 10^9$ decay events.

correspond to the statistics that would be needed to provide the same resolution in an un-weighted histogram. The weighting and calculation of effective counts is handled by the software package's built-in histogram functions.

6.2.2 Interpretation of These Results

As one can see from the above figures, the Doppler shifts due to the total velocity profile is more drastic for a larger value of neutrino mass. Also, the effect of these Doppler shifts is to "straighten out" the Kurie plot of massive neutrinos. One would expect that this effect would lead to a underestimation of the neutrino mass, because smaller dips in Kurie plots ordinarily correspond to smaller neutrino masses (see Chapter 3).

Another interesting fact to note is that the distortion due solely to the flow velocity was approximately one order of magnitude smaller than the distortion due to thermal motion. It is worth considering the origin of this difference to determine whether or not this is an artifact of these simulations. As stated earlier, the velocities predicted by the fluid flow model we are using, Eq. 5.28, are, near the injection point, approximately one order of magnitude smaller than the thermal velocities predicted by Eq. 4.4. Near the ends of the WGTS (large values of $|z|$), however, these velocities are multiple orders of magnitude larger than the thermal velocities. These larger flow velocities should have a much larger effect on the beta spectrum than the thermal velocities.

However, consider Fig. 6.1, which represents the distribution of parent T_2 molecules in our 2D slice of the WGTS. As is expected, the density of tritium is much larger near the injection point than it is near the exit points. This means that there are many more tritium molecules in the region of low flow velocity (small $|z|$, and so, small $\left|\frac{dP}{dz}\right|$ by Fig. 6.1) than there are in the regions of high flow velocity. Thus, decays are much more likely to occur in the region of low flow velocity, near the injection point. Furthermore, due to the higher probability of a random event occurring at a larger radius than a smaller radius, the density of the tritium is higher near the wall of the WGTS than it is near the center (as can also be seen in Fig. 6.1). Due to viscosity, the velocity decreases as the square of the radial distance from the center of the WGTS (Eq. 5.28). Therefore, these higher density regions are also lower velocity regions.

Physically, a molecule near the ends of the WGTS has the largest potential to have a large single effect on the beta spectrum, due to the high velocity. However, this high velocity also means that the molecule spends less time in this region, and so, is less likely to decay there. Thus, we would expect the high energy shifts due to flow velocity to contribute to the beta spectrum in the form of high-energy outliers. In fact, there are outliers visible in the flow-shifted spectra (Figs. 6.2.1, 6.2.1, 6.2.1).

Thus, this model predicts that the low probability of high-velocity decays dominates over the effect of these high-velocities on the beta spectrum. However, is this also true for KATRIN? One important fact to note in the interpretation of this data is that KATRIN produces beta decays at a rate much faster than my simulations can. Thus, with these higher count rates, KATRIN may be sensitive to a level of these outlier high-energy shifts that is simply not present in the number of statistics presented here. To investigate this, one might perform a single simulation for a specific set of parameters, which would, of course yield higher statistics than the preliminary and general study presented here.

I believe that it is also important to note that this suppression of high-velocity decays due to density is exacerbated by the particular density model used in this analysis. The approximate density profile in Fig. 5.1 goes to *zero* at the ends, whereas, in reality the density does not actually reach zero. This artificially suppresses the decay rate at the endpoints, and so, suppresses the effect of the flow velocity. Also, the velocity model that we are using, Eq. 5.28, is being stretched beyond the validity of its assumptions in this region of high-velocity near the endpoints. It seems very likely that the creation of a more accurate density model near the endpoints would go hand-in-hand with a more accurate velocity model in this region, so this could perhaps be a more fruitful route than continuing on with Eq. 5.28.

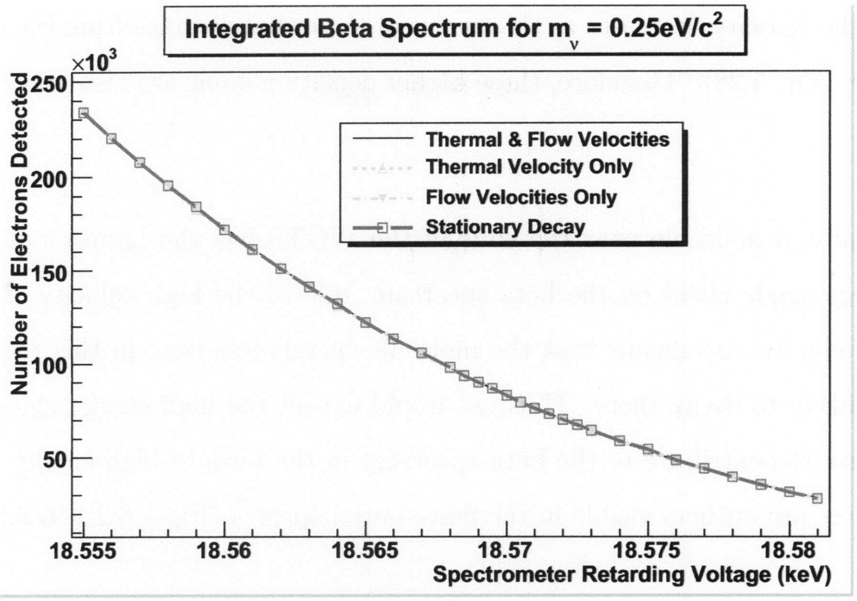

Figure 6-15: The integrated spectra for a neutrino mass of $0.25\text{eV}/c^2$. This figure is simply given as a representative example of the spectra over the entire range that KATRIN will measure; the individual spectra are difficult to distinguish on this scale.

6.3 The Integrated Spectra and Fit Results

As discussed in Chapter 2, the KATRIN spectrometer is an integrating spectrometer. So, to simulate the measurements results that KATRIN might obtain from the above simulated raw spectra, we must integrate the spectra. This integration was done in steps that correspond to the retarding voltages that are planned to be used in the KATRIN measurements.[22] For each retarding voltage, the number of counts with above that energy is tallied, and the resulting number was used as the mean in a Poisson distribution. A number was then drawn from this distribution, and this was the number used as the measured value (the square root of that number was used as an error). The resulting spectra are given here.

These spectra were created to be fed into a fitter, created by graduate student Asher Kaboth, which reports the neutrino mass and endpoint corresponding to a given integrated spectra. [22] The results of this fitter's analysis is summarized in Tables 6.3 and 6.3.

Because the velocity effects shifted both the endpoint and the shape of the spec-

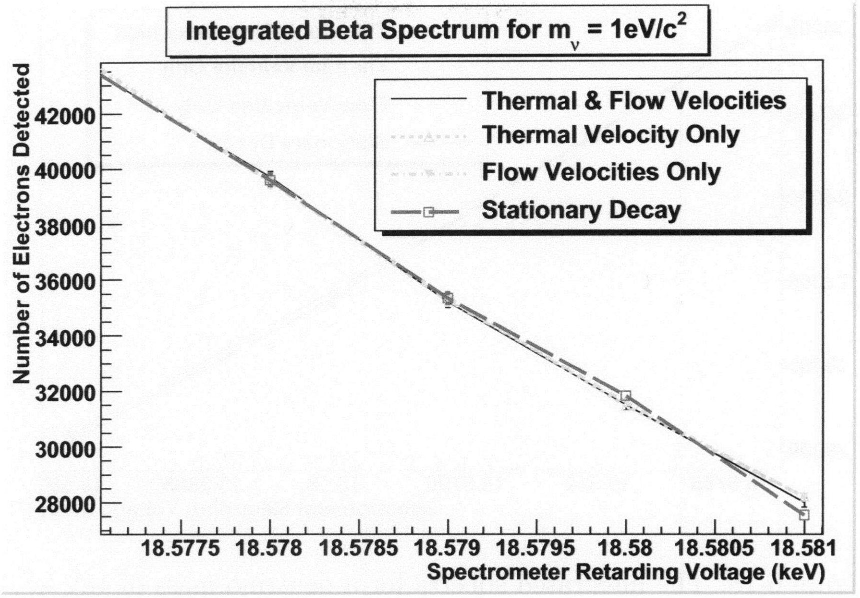

Figure 6-16: The integrated spectra for a neutrino mass of 1eV/c^2.

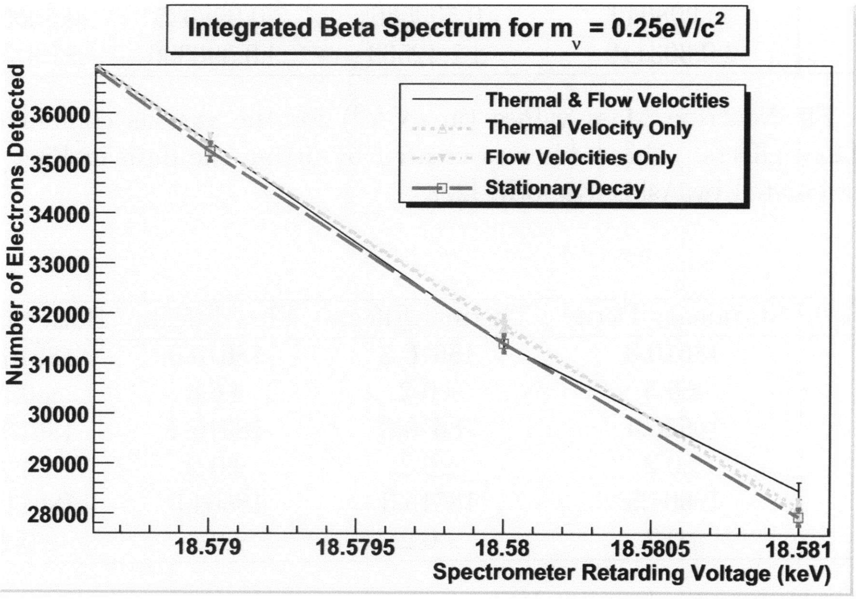

Figure 6-17: The integrated spectra for a neutrino mass of 1eV/c^2.

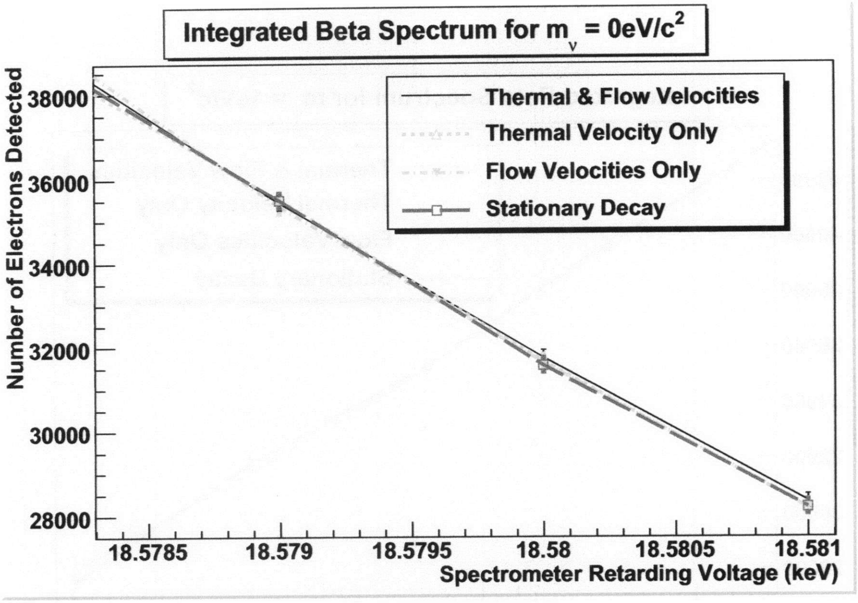

Figure 6-18: The integrated spectra for a neutrino mass of 1eV/c^2.

$m_\nu(eV/c^2)$	Stationary Decay	Thermal Effects	Flow Effects	Both Effects
0	0.00000	-0.999780	0.000000	-0.99977
	±0.733767	±0.880019	±0.746666	±0.824665
0.25	0.299997	-0.998350	-0.299997	-0.998368
	±0.412502	±1.32312	±0.40062	±1.31047
1	-0.998049	0.500566	-0.998035	0.500566
	±0.393119	±1.42563	±0.396306	±1.43557

Table 6.1: Fit Neutrino Mass values (in eV/c^2) for the various combinations of velocity-related effects. This table was created by fitting the data in Figs. 6.3-6.3 with a fitter created by Asher Kaboth. [22]

$m_\nu(eV/c^2)$	Stationary Decay	Thermal Effects	Flow Effects	Both Effects
0	18610.0	18616.8	18610.0	18616.9
	±6.5	±0.2	±6.6	±0.2
0.25	18616.4	18616.8	18616.4	18616.8
	±0.2	±0.2	±0.2	±0.2
1	18604.5	18615.3	18604.5	18611.5
	±0.2	±0.2	±0.2	±0.2

Table 6.2: Fit Endpoint values (in eV) for the various combinations of velocity-related effects. This table was created by fitting the data in Figs. 6.3-6.3 with a fitter created by Asher Kaboth. [22]

trum, the fitting of the above results was made more difficult. In Tables 6.3 and 6.3, the velocity-related effects can be seen to increase the endpoint value, as expected, and as seen in figures in this section also. Another effect of the Doppler shifts is to decrease the fitted value of the neutrino mass. This effect was expected earlier when it was noted that the Doppler shifts have the effect of "straightening out" the Kurie plot.

Chapter 7

Conclusions

The analysis here has shown that the Doppler shifts due to the tritium source motion within the WGTS shift the endpoint of the decay by an amount on the order of 0.2eV. This shift also varies as function of neutrino mass, and is mostly dominated by the random thermal motion of the tritium molecules. In addition to the simple endpoint shift, the actual shapes of the endpoint distortions are presented here.

The effects due to the flow caused by pumping, Eq. 5.28, were shown to be smaller than the effects due to thermal motion by approximately one order of magnitude. Thus, the fluid flow distortion of the endpoint is negligible in these data. This conclusion should apply well to the hydrodynamic region near the injection point. However, the assumptions of the velocity model used in these simulations break down in the free molecular regime near the exit points. This is the very region where the flow velocity effects should be strongest. Therefore, the suppression of high-velocity flow effects present in these data is not necessarily reliable. It may rather point to the inability of this approximated model to capture the true physics of that region of the WGTS. Improved modeling of this *free molecular* region of the WGTS to obtain more accurate density and velocity profiles seems to be necessary to further quantify the effects in this region.

Another effect observed in these simulations was the "washing-out" of the velocity effects by the inclusion of the final state distribution. For the statistics presented here, $5 \cdot 10^9$ events, it was difficult to distinguish the stationary decay spectra from the Doppler shifted spectra in any clear or meaningful way. Further simulations with higher statistics (longer running time and higher computational power) would help determine whether this is simply a result of low statistics or whether the velocity-related effects are truly masked by the final state distribution.

In addition to the specific results of this study, the simulation program created for this study has significant potential for extension to other aspects of the KATRIN simulations being performed. For instance, every run of the simulation creates all three four-vectors of the products of the decay at a weighted location in three-dimensional space (assuming axial symmetry of the WGTS). These products can be directly piped into the GEANT simulations, which simulate the motion and interactions of the particles as they pass through the actual geometry and conditions of the detector. In this way, the interactions between the particles and the energy loss within the apparatus can be simulated with the actual decay products.

Also, the structures used to incorporate the final states of the $(^3HeT)^+$ ion can easily be extended to include the relative mixtures of the various gasses within the source and also the final states of other decay products, such as those presented for $(^3HeH)^+$ in Ref. [14]. In addition to this, because the simulation is starts from the general decay model, takes for input only the rest-masses of the relevant particles, and so, can be easily modified to simulate the other decays that take place in the WGTS.[6]

Appendix A

Simulation Code

```
/* For readability, the code included here is the less general version of the
code, which is custom-tailored to the calculations performed in this thesis.
Presented here is the general loop structure that simulates the decay.
Simulating the various combinations of velocity effects simply consists of
turning off and on various boostings.
It uses histograms that were created by other pieces of code, which contain
the Pressure/Density profile, the Final States Distribution, and the
derivative of the Pressure/Density Profile.

Not presented here is the code that analyzes/plots the data and Kurie plots,
or the code that creates the histograms used in this code snippet.
*/


#include <iostream>
#include <string>
#include <math.h>
#include <fstream>
#include "TLorentzVector.h"
#include "TCanvas.h"
#include "TGenPhaseSpace.h"
```

```
#include "TRandom3.h"
#include "TGraph.h"
#include "TFile.h"
#include "TTree.h"
#include "TH1D.h"
#include "TF1.h"
#include "TVector3.h"
#include "TMath.h"

using namespace std;

//Global Variables for Distributions
TRandom3 RN; //Random Number Generator
TF1 RCirc("RadDistrib","x",0,1);//Radial Distribution
TH1D * hP = new TH1D; //Pressure profile
TH1D * hdPdz = new TH1D;//Derivative of Pressure profile
TH1D * hFS = new TH1D; //Final State Distribution

//---Initialize the Distribution Histograms ----------------
void InitPDistrib(){
TFile *f = new TFile("PresProf.root");
hP = (TH1D*)f->Get("P");
hdPdz = (TH1D*)f->Get("dPdz");
}
void InitFSDistrib(){
TFile *f = new TFile("FinStates.root");
hFS = (TH1D*)f->Get("FinStates");

}
void InitHistograms(){
```

```
InitPDistrib();
InitFSDistrib();
}
//------------------------------------------------------------

struct weights_t{
//Contains the various Weighting info for the event
Double_t FullWeight;
Double_t TGenWeight;
Double_t DotProduct;
Double_t FermiFunc;
};

inline Double_t GetU(Double_t y, Double_t z){
//Returns Beta factor of viscous, 2D veolcity profile
//y = r in the coordinates used in this thesis
//z = position along WGTS axis
//PBinLength = Width of bins in hP histogram

  Int_t BinNum = floor(abs(z)/PBinLength)+1; //Convert z to Bin#
  Double_t N = hP->GetBinContent(BinNum); //Get the Density
  Double_t dNdz = hdPdz->GetBinContent(BinNum); //Get the derivative
    if(z < 0) dNdz = -1 * dNdz; //Handle the symmetry of the provile

  Double_t A = (mu/Pin)*sqrt((pi*kb*T)/(2*m))*(1/N);
  Double_t B = (pi*d*mu*kb*T)/(m*Pin*Pin*(2*A + sqrt(3)*d))*(1/(N*N));
  Double_t u = -(Pin/(2*mu))*(dNdz)*(d*d/4 - (y*y) + d*A + 2*mu*B);
  return u/c;
};
```

```
inline TVector3 RandomDir(){
Double_t x, y, z;
RN.Sphere(x, y, z, 1);
TVector3 temp(x, y, z);
return temp;
};

inline Double_t Fermi(Int_t Z, Double_t B){//Fermi Function
//Z = Nuclear Charge, B = Beta factor of electron
//Fa = Fine Structure Constant, a0 & a1 are the emperical values
Double_t x = (2*pi*Z*Fa)/B;
Double_t temp = x/(1-exp(-x))*(a0+a1*B);
return temp;
};
inline Double_t FP(Int_t Z, TLorentzVector P){
//Computes Fermi Function given a 4-vector of electron, P
Double_t bf = P.BoostVector().Mag();
Double_t temp = Fermi(Z, bf);
return temp;
};

//Maxwell Speed Distribution----------------------------------
Double_t MaxBeta=5e-6;
TF1 *MSpeedB = new TF1("MaxwellSpeedB", "x*[3]*x*[3]*exp(-([0]*x*[3]*x*[3])
/(2*[2]*[1]))", 0, MaxBeta);

//Initialize Values of Maxwell Speed Distribution
void SetMSpeedParams(TF1 *MSpeedB, Double_t Temp=27){
//0 = mass, 1 = Temperature, 2 = kb (Boltzmann's constant)
MSpeedB->SetParameter(0, Mthermal);
```

```
MSpeedB->SetParameter(1, Temp);
MSpeedB->SetParameter(2, kb);
//MSpeedB->SetParameter(3, 1); //For speeds in mks
MSpeedB->SetParameter(3, c); //For speeds as Beta Factors
};//--------------------------------------------------------------

inline void GetPosition(Double_t &r, Double_t &z){
//Pick a location for a decay event based on the 2D geometry and the density
distribution
//d = diameter of WGTS, r & z as defined in thesis
r = (d/2) * RCirc.GetRandom();
z = hP->GetRandom();
if(RN.Uniform(0,1) < 0.5) z = -1 * z;//Pick z<0 or z>0
};

inline TVector3 GetVt(){
//Gets the Thermal Velocity (hard-coded for Maxwell-Speed)
Double_t vmag = MSpeedB->GetRandom();
TVector3 temp = RandomDir();
temp = temp * vmag;
return temp;
};



//----------------------------------------------------------------
//Sample of the general boosting routine with All boosting options (thermal
and flow velocity) turned ON.

void WithBoostL(Int_t NumTimes, Double_t NeutrinoMass, string Nme,
Int_t NumBins = 1e6, Double_t Temp=27) {
```

```
//NumTimes = # times to execute loop, Nme = Name of the Run
//NeutrinoMass = electron antineutrino mass in eV
//NumBins = # Bins the Beta Spectrum Histogram should have
//Temp = temperature of WGTS

  InitHistograms();
  SetMSpeedParams(MSpeedB, Temp);

  string HistNme = "h" + Nme + "WB";
  TH1D *h2 = new TH1D(HistNme.c_str(),"Electron Energy Spectrum;Electron
Kinetic Energy (keV)", NumBins, 0, 19);

  TLorentzVector W(0.0, 0.0, 0.0, MParent);
//For TGenPhaseSpace, {Momentum, Energy} units are {Gev/C, GeV}
  if(NeutrinoMass!=0) NeutrinoMass=(1e-9)*NeutrinoMass;//Convert Units
  //masses[] contains the rest-masses of the products
    //(masses[2] is changed later by Final States Distribution
  Double_t masses[3] = { NeutrinoMass, Me, MDaughter};

  TVector3 Vt(0,0,0), U(0,0,0), BoostV(0,0,0);
  Double_t r=0, z=0, Uz=0;
  weights_t wt;


//For use with TTrees (not used in thesis calculations)
//This is may be used for detailed particle tracking
  //TLorentzVector Neu, El, He;
  //TTree Tr("Tr", "Results");
  //Tr.Branch("Electron",&El[0],"Px/D:Py:Pz:E");
  //Tr.Branch("Neutrino",&Neu[0],"Px/D:Py:Pz:E");
  //Tr.Branch("He",&He[0],"Px/D:Py:Pz:E");
  //Tr.Branch("Position",&Position[0],"x/D:y:z");
  //Tr.Branch("BoostVelocity",&BoostV[0],"Vx/D:Vy:Vz");
//Tr.Branch("Weights",&wt,"FullWeight/D:TGenWt:DotProduct:FermiFunc");

  //The ROOT General Phase-Space Decay
  TGenPhaseSpace event; event.SetDecay(W, 3, masses);


  for(Int_t i=0; i < MaxI; i++){

    masses[2] = MDaughter + (hFS->GetRandom()); //Final State
    event.SetDecay(W, 3, masses); //Distribution

    wt.TGenWeight = event.Generate(); //Simulate Decay

    TLorentzVector *pNeutrino = event.GetDecay(0);
    TLorentzVector *pElectron = event.GetDecay(1);
    //TLorentzVector *pHe = event.GetDecay(2);//Not used in thesis

    wt.FermiFunc = FP(2, *pElectron); //Fermi Function Weighting
    wt.DotProduct = pElectron->Dot(*pNeutrino);//Dot-Product Weighting
    wt.FullWeight = wt.TGenWeight * wt.DotProduct * wt.FermiFunc;

    GetPosition(r, z); //Get Decay Position in 2D space
    Uz = GetU(r, z);    U.SetZ(Uz); //Get Flow Velocity
    Vt = GetVt(); //Get Thermal Velocity
    BoostV = Vt + U;

    pElectron->Boost(BoostV);
//  pNeutrino->Boost(BoostV); //Not used
//  pHe->Boost(BoostV); //in thesis

    //Fill Beta Spectrum Histogram
    h2->Fill((pElectron->E() - masses[1])*1e6, wt.FullWeight);

    //For Use With TTrees (not used in thesis)
    //Neu = *pNeutrino;
    //El = *pElectron;
    //He = *pHe;
    //Tr.Fill();



  };

  Nme += "WB.root";
  TFile f(Nme.c_str(), "RECREATE");
  //Scale the Histogram to yield Effective Entries
  h2->Scale((h2->GetEffectiveEntries())/(h2->Integral()));
    h2->Write();
  f.Close();

};
```

Bibliography

[1] D. J. Griffiths *Introduction to elementary particles.* Wiley. New York: 1987.

[2] P. Marmier and C. Sheldon *Physics of Nuclei and Particles.* Academic. New York: 1969.

[3] J.N. Bahcall and R. Davis Junior. *Solar Neutrinos: The First Thirty Years.* Addison-Wesley. Reading, Massachusetts: 2004.

[4] F. Boehm and P. Vogel. *Physics of Massive Neutrinos.* Cambridge University Press. Cambridge: 1987.

[5] R. Shankar *Principles of Quantum Mechanics, Second Edition.* Yale. New Haven: 1994.

[6] J. Angrik, et. al. *KATRIN Design Report 2004.* FZKA Scientific Report, 2004.

[7] S. Hannestad, "Neutrinos in cosmology," New J. Phys. 6 (2004) 108, arXiv:hep-ph/0404239

[8] S. Hannestad, astro-ph/0404239

[9] K. Valarius. *Status of Direct Neutrino Mass Measurements and the KATRIN Project.* International Europhysics Conference on High Energy Physics, 2005.

[10] F. Sharipov, KATRIN internal report 10-ME-2102.

[11] S. Masood, et. al. *Exact relativistic beta decay endpoint spectrum* arXiv:0706.0897v1 [hep-ph].

[12] J.J. Simpson, Phys. Rev. D23 (1981) 649.

[13] H. Behrens and J. Jaenecke, *Landolt-Boernstein New Series.* Springer. Berlin: 1969.

[14] A. Saenez, S. Jonsell, and P. Froelich, Phys. Rev. Lett. 84 (2000) 2

[15] N. Doss and J. Tennyson, Phys. Rev. C73 (2006) 025502

[16] F. Reif *Fundamentals of Statistical and Thermal Physics.* McGraw Hill. New York: 1965.

[17] K. Essig and T. Thuemmler, KATRIN internal report 25-ME-7001-2

[18] K. Essig, *private communication*

[19] F. Sharipov and V. Seleznev, "Rarefied gas flow through a long tube at any pressure ratio," V. Vac. Sci. Technol. A 12 (1994) 2933-2935.

[20] F. Sharipov and V. Seleznev, "Data on internal rarefied gas flows," J. Phys. Chem. Ref. Data 27 (1998) 657-706.

[21] F. Sharipov, *private communication*

[22] A. Kaboth *private communication*

[23] K. Huang *Introduction to Statistical Physics.* CRC Press. New York: 2001.

[24] R. Baierlein *Thermal Physics.* Cambridge University Press. New York: 1999.

[25] K. Huang *Statistical Mechanics.* Wiley. New York: 1987.

[26] S. Shen and G. Chen, "A kinetic-theory based on first order slip boundary condition for gas flow," Physics of Fluids 19 (2007) 086101.